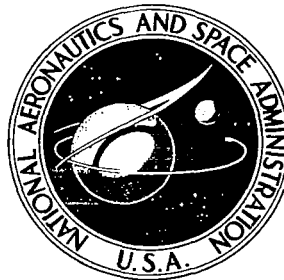


# NASA CONTRACTOR REPORT

NASA CR-2688



NASA CR-2688

0061494



LOAN COPY: RETURN TO  
AFWL TECHNICAL LIBRARY  
KIRTLAND AFB, N. M.

## VALIDATION OF SCRAMJET EXHAUST SIMULATION TECHNIQUE

*H. B. Hopkins, W. Konopka, and J. Leng*

*Prepared by*

GRUMMAN AEROSPACE CORPORATION

Bethpage, N.Y. 11714

*for Langley Research Center*



NATIONAL AERONAUTICS AND SPACE ADMINISTRATION • WASHINGTON, D. C. • JUNE 1976



0061494

1. Report No. NASA CR-2688		2. Government Accession No.		3. Recipient's Catalog No.	
4. Title and Subtitle  VALIDATION OF SCRAMJET EXHAUST SIMULATION TECHNIQUE				5. Report Date June 1976	
				6. Performing Organization Code	
7. Author(s) H. B. Hopkins, W. Konopka, and J. Leng				8. Performing Organization Report No. RE-509	
9. Performing Organization Name and Address Grumman Aerospace Corporation Bethpage, NY 11714				10. Work Unit No. 505-11-31-02-00	
				11. Contract or Grant No. NAS1-13089	
12. Sponsoring Agency Name and Address National Aeronautics and Space Administration Washington, DC 20546				13. Type of Report and Period Covered CONTRACTOR REPORT	
				14. Sponsoring Agency Code	
15. Supplementary Notes Langley technical monitor: James L. Hunt  Final report.					
16. Abstract  Scramjet/airframe integration design philosophy for hypersonic aircraft results in configurations having lower aft surfaces that serve as exhaust nozzles. There is a strong coupling between the exhaust plume and the aerodynamics of the vehicle, making accurate simulation of the engine exhaust mandatory. This report describes the experimental verification of the simulation procedure devised by Grumman Research during a previous NASA contract (CR-2494). The detonation tube simulator was used to produce an exact simulation of the scramjet exhaust for a Mach 8 flight condition. The pressure distributions produced by the "exact" exhaust flow were then duplicated by a cool mixture of Argon and Freon 13B1. Such a substitute gas mixture validated by the detonation tube technique could be used in conventional wind tunnel tests. The results presented in this report show the substitute gas simulation technique to be valid for shockless expansions.					
17. Key Words (Suggested by Author(s)) Engine/Airframe Integration Hypersonics Simulation Scramjet				18. Distribution Statement  Unclassified - Unlimited  Subject Category 05	
19. Security Classif. (of this report) Unclassified	20. Security Classif. (of this page) Unclassified	21. No. of Pages 83	22. Price* \$4.75		



## TABLE OF CONTENTS

<u>Section</u>	<u>Page</u>
1      Introduction and Summary .....	1
2      Detonation Tube Simulator .....	3
Detonation Tube/Combustor Nozzle Design ....	6
Cowl and Afterbody Model Design .....	9
Instrumentation .....	16
Data Acquisition and Reduction .....	21
Flow Visualization .....	21
3      Detonation Tube Running Conditions .....	24
Combustion Gas ( $\phi = 1.0$ ) .....	24
Substitute Gas .....	24
4      Afterbody Flow Field Predictions .....	29
Side Expansion (Three Dimensional) Effects .	30
Model Geometry Effects .....	34
5      Experimental Results .....	38
Pressure Distributions .....	38
Combustion Products .....	38
Substitute Gas Comparison .....	45
Heat Transfer .....	50
Infrared Radiation from Nozzle Exit Plane ..	50
Impact Pressure Measurements .....	55
6      Conclusions and Recommendations .....	61
7      References .....	62

Appendices:

A	On the Calculation of the Properties of Substitute Gas Mixtures .....	64
B	Experimental Pressure Data Normalized by Nozzle Exit Pressure, $P_3$ .....	69

# LIST OF ILLUSTRATIONS

<u>Figure</u>		<u>Page</u>
1	Detonation Tube Simulator Schematic .....	4
2	Photograph of Detonation Tube Simulator .....	5
3	Detonation Tube $\frac{1}{8}$ Scale, Combustor Nozzle Centerline Mach Number Distribution .....	10
4	Combustor Nozzle Exit Plane Mach Number Distribution .....	11
5	Detonation Tube Contoured Nozzle Exit Plane Flow Angularity .....	12
6	Gauge Locations - Afterbody Model .....	13
7	Cross Section and Gauge Locations-Cowl Model ....	14
8	Photograph of Model Mounted in Test Section .....	15
9	Model with Short Side Plates .....	17
10	Model with Long Side Plates .....	17
11	Static Calibration of $1.38 \times 10^5 \text{ N/m}^2$ Pressure Transducer No. 3-8 .....	20
12	Pressure Trace for Run with Combustion Products Indicating Increased Noise Due to Flow .....	22
13a	Oscilloscope Record of Detonation Tube Stagnation Pressure, $P_5$ (Two Independent Transducers) .....	25
13b	Oscilloscope Record of Combustor Nozzle Exit Plane Static Pressure, $P_3$ , Combustion Run .....	25
14a	Oscilloscope Record of Substitute Gas Reflected Shock Stagnation Pressure, $P_5$ (Two Independent Transducers) .....	28

<u>Figure</u>		<u>Page</u>
14b	Oscilloscope Record of Combustor Nozzle Exit Plane Static Pressure, $P_3$ , Substitute Gas Run ...	28
15	Theoretical, Two Dimensional, Afterbody Pressure Distributions .....	31
16	Typical Two Dimensional Afterbody Pressure Distribution on the Centerline Corrected for Nozzle Side Expansion Effects .....	33
17	Characteristics Drawing Showing Expansion and Shock Wave from Combustor Exit .....	35
18	Afterbody Surface Pressure Distribution Showing Pressure Perturbation Due to a Two Degree Expansion and Recompression .....	36
19	Pressure Distribution on Afterbody Centerline - Comparison of Results with and without Step at Nozzle Cowl Joint .....	40
20	Pressure Distribution on Cowl - Combustion Runs and Comparison with 2-D M-O-C Calculation ..	41
21	Planform View of Afterbody Showing Ideal and Measured Two Dimensional Regions - No Side Plates .....	42
22	Pressure Distribution on Afterbody Centerline with and without Short Side Plates - Combustion Runs .....	43
23	Planform View of Afterbody Showing Measured and Ideal Two Dimensional Region - Short Side Plates .....	44
24	Pressure Distribution on Afterbody-Combustion Runs - Short and Long Side Plates - Comparison with 2-D M-O-C Calculation Assuming Two Degree Ramp at Nozzle-Cowl Joint .....	46
25	Cowl Pressure Distribution - Comparison of Combustion with Substitute Gas Results .....	48

<u>Figure</u>		<u>Page</u>
26	Afterbody Centerline Pressure Distributions - Comparison of Combustion with Substitute Gas Results - Short Side Plates .....	49
27	Afterbody Centerline Pressure Distribution for Substitute Gas Run Through Off-Design Nozzle .....	51
28	Heat Transfer Distribution Along Afterbody Centerline .....	53
29	Comparison of Calculated and Measured Infrared Emission from Nozzle Exit Plane .....	54
30a	Oscilloscope Record of Combustion Gas Impact Pressure at Nozzle Exit Plane .....	56
30b	Oscilloscope Record of Substitute Gas Impact Pressure at Nozzle Exit Plane .....	56
31	Ratio of $P_{T1}/P_{T2}$ Versus Mach Number for Different Values of $\gamma$ (Ideal Gas) .....	57
A-1	Variation of $C_p$ with Temperature for Mixture of 42% Argon and 58% Freon 13B1 .....	67



## SYMBOLS

Ar	argon atom
a	sound speed
Br	bromine atom
C	carbon atom
$C_p$	specific heat at constant pressure
$C_v$	specific heat at constant volume
F	fluorine atom
Freon 13B1	bromotrifluoromethane ( $\text{CBrF}_3$ )
H	enthalpy; also hydrogen atom
h	static enthalpy
K	Kelvin temperature scale
k	prefix "kilo" ( $10^3$ )
M	Mach number ( $\equiv U/a$ )
M-O-C	method of characteristics
m	unit of length (meter); also prefix "milli" ( $10^{-3}$ )
N	nitrogen atom; also unit of force (Newton)
O	oxygen atom
P	pressure
$\dot{Q}$	heat transfer rate
R	specific gas constant
T	temperature

U	velocity
X	distance measured along detonation tube and combustor axis (vehicle roll axis); also mole fraction of a chemical specie
$\bar{X}$	nondimensional distance ( $\equiv X/Y_3$ )
Y	vehicle yaw axis
$\bar{Y}$	nondimensional distance ( $\equiv Y/Y_3$ )
Z	vehicle pitch axis
$\alpha$	angle of attack
$\beta$	inlet ramp angle
$\gamma$	ratio of specific heats, $c_p/c_v$
$\theta$	flow angle relative to X axis
$\mu$	prefix "micro" ( $10^{-6}$ )
$\rho$	density
$\phi$	equivalence ratio

### Subscripts

o	refers to total (stagnation) condition
1	refers to an arbitrary thermodynamic state point; also initial, unburned gas conditions in driven tube
2	refers to an arbitrary thermodynamic state point
3	refers to combustor exit plane
4	refers to unexpanded, high pressure driver gas
5	refers to stagnation condition or region behind reflected shock wave in detonation tube

$\infty$  refers to undisturbed free stream

$i$  refers to  $i^{\text{th}}$  chemical specie; also internal flow

$T_1$  total or stagnation conditions upstream of a shock wave

$T_2$  total or stagnation conditions downstream of a shock wave

# VALIDATION OF SCRAMJET EXHAUST SIMULATION TECHNIQUE

H. B. Hopkins, W. Konopka, and J. Leng

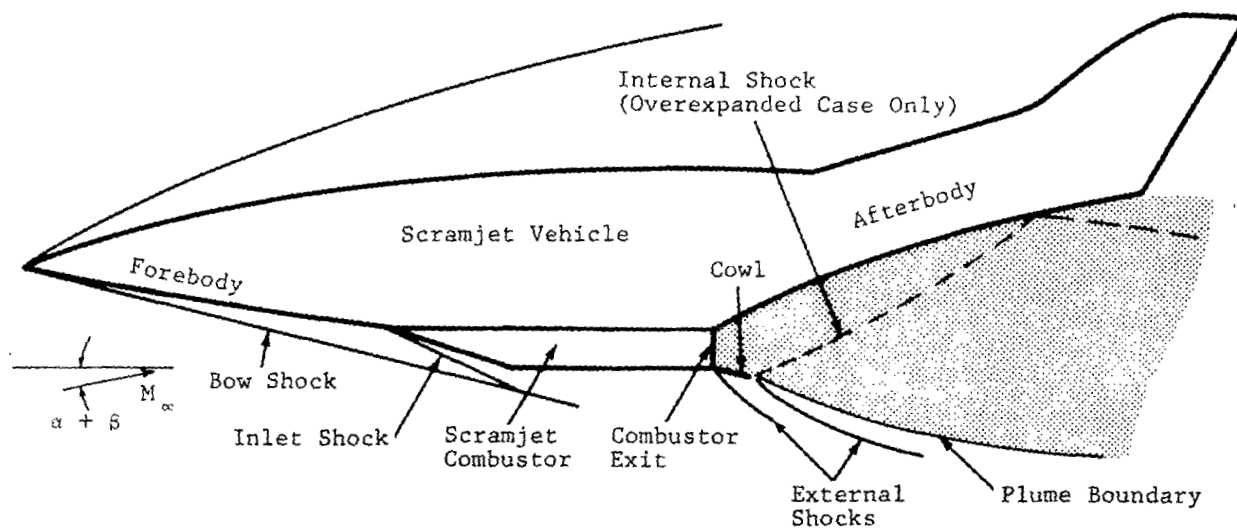
Grumman Aerospace Corporation

## 1. INTRODUCTION AND SUMMARY

The present concept of a scramjet-powered hypersonic vehicle employs a hydrogen burning engine integrated beneath the fuselage as shown in the sketch below. It is apparent from such a design that the engine exhaust gases will play a major role in the determination of the aerodynamic forces and moments on the vehicle. Calculations of such flows involve many simplifying assumptions thus making it mandatory to obtain experimental data for design purposes. One of the most difficult simulation problems for the scramjet exhaust is to reproduce the effect of the correct chemistry along with the high total enthalpy (flight compression plus combustion heating) in the exhaust flow. To achieve this combination with the true combustion mixture in a conventional wind tunnel model of reasonable complexity is a virtual impossibility. Late in 1973 a study was conducted to select a technique for scramjet exhaust simulation that had the best chance for success (Ref. 1). At the conclusion of that study it was proposed that the most practical method would be the use of substitute gases having thermodynamic properties so as to behave in a manner similar to the reacting gas flow from the combustor of a full scale vehicle. Such substitute gases could be validated by an exact laboratory simulation in a unique facility called a detonation tube simulator. This device is ideally suited to scramjet simulation because it combines shock heating of the gas with the heat of combustion to obtain the required total enthalpy.

This report describes experiments and associated analyses aimed at proving the above simulation concept. Scramjet combustor exit plane conditions for a flight Mach number of 8 were duplicated in the facility, and pressure and heat transfer measurements were obtained over a simulated vehicle afterbody and cowl. One substitute gas blend of 42 percent Argon and 58 percent Freon 13B1 was also run for comparison. In addition, impact pressure surveys were conducted in the flow field of both gases, and a measurement of the infrared radiation from the combustion exhaust was used to assess the accuracy with which the desired state of the exhaust products had been achieved.

Results show the concept to be valid. Pressures measured after a 20 degree expansion were normalized to the static pressure at the nozzle exit, and the ratios agree well among the combustion products, substitute gas, and predictions in the two dimensional regions of the flow. The pressures are relatively insensitive to small changes in thermodynamic properties of the gases, but are very sensitive to flow perturbations caused by nozzle or model nonuniformities. The radiation measurements agree well with predictions made before the tests.



## 2. DETONATION TUBE SIMULATOR

The Grumman detonation tube simulator used for the measurement of exhaust flows and validation of the substitute gases is capable of giving nearly correct chemistry and total enthalpy for the hydrogen/air combustion system throughout the entire proposed flight regime. Reynolds numbers can easily be maintained at flight values by running at elevated pressures with both combustion and substitute gases. A schematic of the detonation tube facility is shown in Fig. 1. It consists of a 6.1 meter long, 7.62 cm inside diameter driver section initially separated from a 10 meter long, 12.7 cm inside diameter driven tube by a metallic diaphragm. The driven tube is terminated by a supersonic nozzle designed to produce a flow that will match the expected exit plane conditions of the proposed scramjet engine. The nozzle exhausts into a 1.83 meter diameter, 3.66 meter long test section. Mounted within the section, and mating to the supersonic nozzle is the model afterbody. For the current proof-of-concept experiments, the upper afterbody surface is a flat plate instrumented with 33 pressure transducers and 11 heat transfer gauges. A photograph of the facility is shown in Fig. 2. The test section can be evacuated prior to a run to any desired pressure down to  $5 \times 10^{-5}$  torr. The facility has been designed to handle combustible hydrogen mixtures safely. Various interlocks and leak detection devices are incorporated into the automatic gas handling system. Details of this system may be found in Ref. 2.

Two modes of detonation tube operation are possible. In the first, called the incident or forward-running detonation technique (Ref. 3), the driver section is pressurized with helium to a pressure high enough to ensure detonation of the combustible gases when the main diaphragm ruptures. The diaphragm is scribed to a predetermined depth so that it will rupture at a specific pressure. The shock wave formed will rapidly become a self-propagating detonation wave that will reflect from the nozzle end of the driven tube as a shock wave. The gas is heated and pressurized by the combustion behind the detonation wave and further by the energy addition behind the reflected shock wave. A weak diaphragm at the entrance to the nozzle is ruptured by the arrival of the incident wave and the high energy slug of gas expands through the nozzle into the test section. In order to prevent the rapid expansion that exists behind a free-running detonation wave, the initial helium driver gas pressure is chosen so that when it expands after the rupture of the diaphragm its pressure matches that

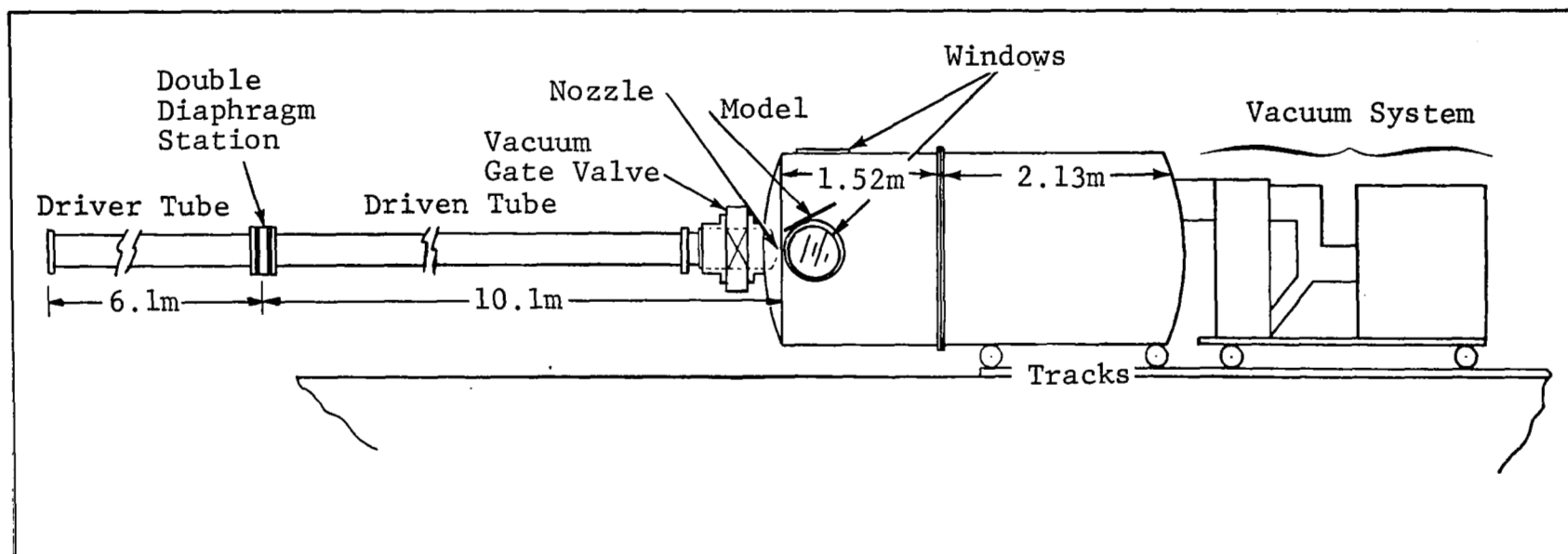
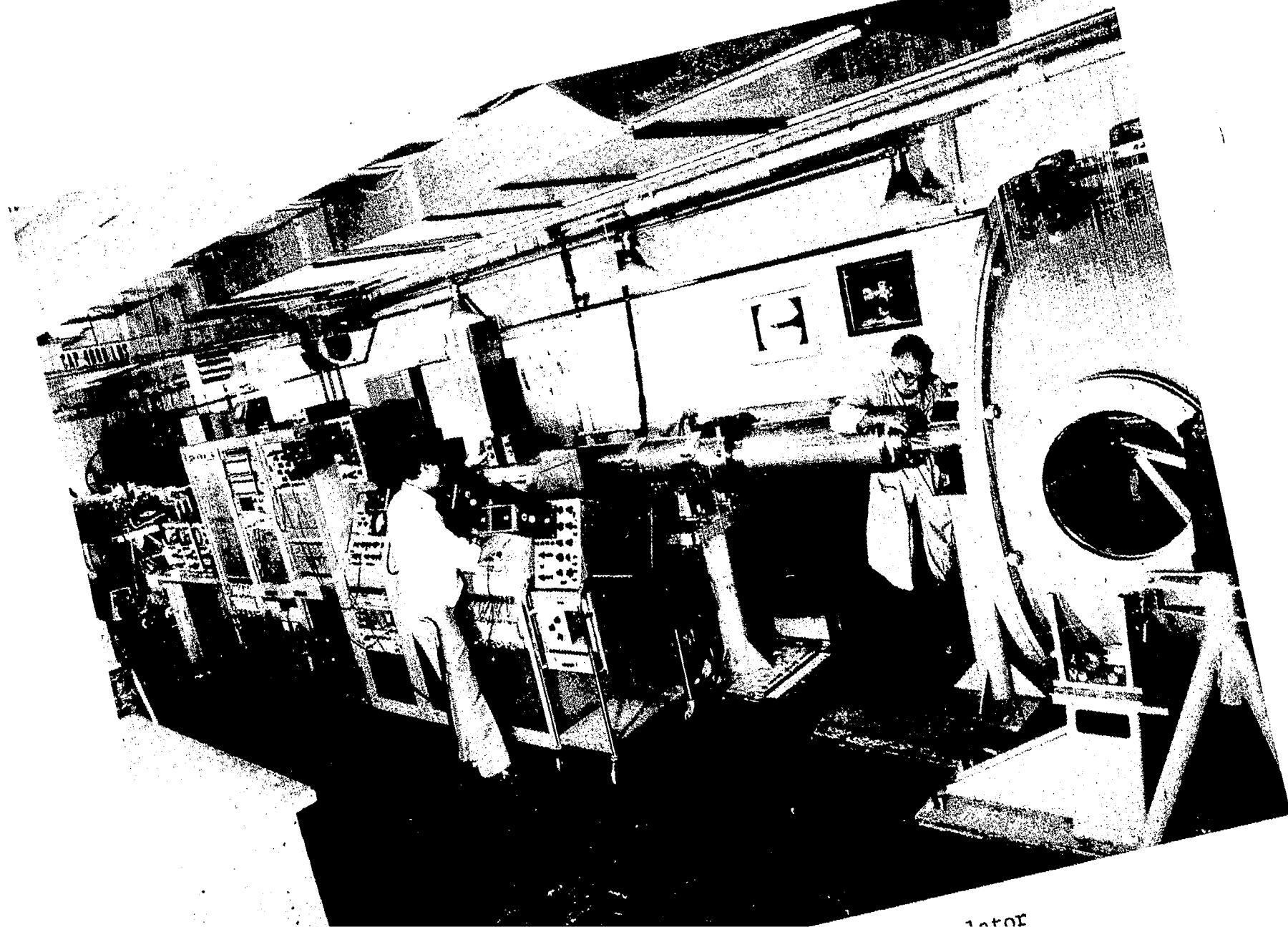


Fig. 1 Detonation Tube Simulator Schematic



1000



immediately behind the detonation wave. This produces quasisteady flow conditions for two to four milliseconds.

The second mode of operation is called the backward-running detonation technique and was used exclusively for the current experiments. This technique was developed specifically for the simulation of hydrogen/oxygen rocket engine plumes (Ref. 2) where the incident technique would have produced an enthalpy higher than the actual engine case because of the shock wave heating added to the heat of combustion. A very weak shock wave is sent into the combustible mixture in this method (through the use of a low driver pressure and weak main diaphragm). The idea is to prevent ignition on the incident wave, but have the gas ignite when the incident wave reaches the nozzle end of the tube. The detonation wave then travels away from the nozzle back towards the driver section. The expansion following this wave drops the pressure and enthalpy in the test gas, which then expands through the nozzle. We have found in previous work (Ref. 2) that the ignition at the end of the tube is best accomplished by a timed electrical spark, although under certain conditions spontaneous ignition behind the reflected wave will occur.

For running the inert substitute gases in the detonation tube we run the facility as a conventional reflected shock tunnel. That is, the test gas mixture is placed in the driven tube. Helium driver gas is used. The shock wave formed on rupture of the main diaphragm reflects from the nozzle end of the driven tube to produce a slug of high energy gas which expands through the nozzle into the test section. The stagnation conditions of the substitute gas are determined by the strength of the incident shock wave in the driven tube, which may be easily controlled.

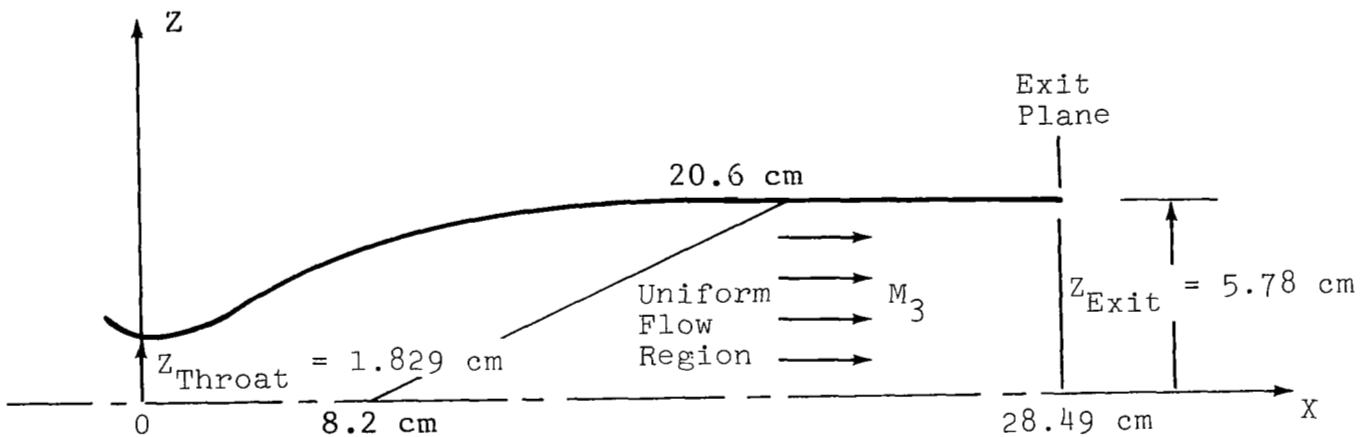
#### Detonation Tube/Combustor Nozzle Design

To duplicate the exit flow of the scramjet combustor in the detonation tube facility, a  $\frac{1}{8}$  scale, two dimensional supersonic nozzle was designed. The prescribed (Ref. 1) nominal combustor exit height was 3.81 cm ( $1\frac{1}{2}$ -in.) and the exit width was 11.43 cm ( $4\frac{1}{2}$ -in.).

We used equilibrium real gas thermodynamics properties generated by the method of Ref. 4 for all the flow field calculations for the combustion products. The method of characteristics program of Ref. 5 was used to design the nozzle to produce the exit

conditions for the  $\alpha + \beta = 4^\circ$  case specified on page 46 of Ref. 1.

The equations developed for the final contour are given below (see sketch) and the X and Z coordinates are given in Table 1. Figure 3 shows the centerline Mach number distribution for this nozzle. The ideal stagnation conditions are  $\phi = 1$ ,  $\alpha + \beta = 4^\circ$ ,  $P_5 = 66.96$  atm,  $H_5 = 578.4$  cal/gm.



Sketch of Contoured Nozzle

Contour Equations  
(all dimensions in inches)

$Z^\dagger = -1.73925X^4 + 1.73925X^3 + 0.72$	$0 \leq X \leq 0.5$
$Z = -0.016528X^3 + 0.024792X^2 + 0.422417X + 0.613363$	$0.5 \leq X \leq 1.0$
$Z = -0.0085214X^3 - 0.0045935X^2 + 0.457168X + 0.599991$	$1.0 \leq X \leq 1.75$
$Z = 0.0013094X^3 - 0.053028X^2 + 0.535855X + 0.557933$	$1.75 \leq X \leq 3.0$
$Z = 0.0027720X^3 - 0.063858X^2 + 0.561343X + 0.539445$	$3.0 \leq X \leq 4.0$
$Z = 0.0016840X^3 - 0.051337X^2 + 0.513396X + 0.600525$	$4.0 \leq X \leq 6.0$
$Z = 0.0009812X^3 - 0.039539X^2 + 0.447730X + 0.7216135$	$6.0 \leq X \leq 8.11$
$Z = 2.2755$	$8.11 \leq X \leq 11.216$

The subsonic inlet radius of curvature is 0.635 cm (0.25 in.).

---

<sup>†</sup>The first of the contour equations is of the form

$$Z = Z_0 + X_1 \tan \theta_1 \left( \frac{X}{X_1} \right)^3 \left( 1 - \frac{X}{2X_1} \right)$$

where  $Z_0$  is throat height,  $\theta_1$  is the maximum expansion angle, and  $X_1$  is the  $X$  value at  $\theta_1$ .

$$X_1 = 2(Z_1 - Z_0) \cot \theta_1$$

This equation is ideally suited for the initial expansion region of wind tunnel nozzles because the first and second derivatives are zero at not only  $X = 0$ , but also at  $X = X_1$  (Ref. 6). For our nozzle we chose  $Z_0 = 1.829$  cm (0.72 in.),  $\theta_1 = 23.5^\circ$ , and  $X_1 = 1.27$  cm (0.5 in.).

TABLE 1 CONTOUR NOZZLE COORDINATES

X(cm)	Z(cm)	X(cm)	Z(cm)	X(cm)	Z(cm)
0	1.8288	3.8705	3.1897	12.9088	5.3462
0.1524	1.8298	4.3249	3.3604	13.9012	5.4577
0.2548	1.8329	5.1181	3.6401	14.8458	5.5466
0.5240	1.8595	5.7277	3.8395	15.7099	5.6144
0.7684	1.9141	6.4094	4.0475	16.4884	5.6650
1.0239	2.0015	7.1610	4.2583	17.4770	5.7150
1.2677	2.1039	7.9926	4.4701	18.3855	5.7480
1.5591	2.2306	8.8930	4.6761	19.0150	5.7638
1.9731	2.4097	9.8458	4.8699	19.6517	5.7742
2.2167	2.5143	10.3490	4.9632	20.3040	5.7793
2.4841	2.6281	10.8506	5.0498	20.8679	5.7798
3.1039	2.8859	11.8839	5.2100	28.4879	5.7798

The extent of the exit plane nonuniformities calculated for this nozzle is illustrated in Figs. 4 and 5 where we show the exit plane Mach number and flow angularity distributions for the  $\alpha + \beta = 4^\circ$ , and  $\alpha + \beta = 12^\circ$  cases for the combustion gas, and for the substitute gas (42 percent Argon, 58 percent Freon 13B1) designed to simulate the  $\alpha + \beta = 12^\circ$  case. For the substitute gas, thermodynamic data were generated by the procedure described in Appendix A. These nonuniformities seem quite small, but note that as the thermodynamic properties of the gas deviate further and further from that for which the contour was designed, the nonuniformities grow stronger. It appears that there is a weak disturbance in the middle of the nozzle which is barely perceptible with the design gas, but becomes stronger with off-design gases.

#### Cowl and Afterbody Model Design

The model afterbody is a flat plate mounted at a angle of 19.76 degrees from the bottom edge of the nozzle. It is 76.835 cm long (30.25 in.) and has a span of 50.8 cm (20 in.). There are locations for 38 pressure transducers and 11 heat transfer gauges as shown in Fig. 6.

The cowl cross section is shown in Fig. 7. It is 11.887 cm (4.68 in.) long and also has a span of 50.8 cm (20 in.). There are locations for 15 pressure transducers and 7 heat transfer gauges in the cowl model as shown in Fig. 7. Figure 8 is a photo-

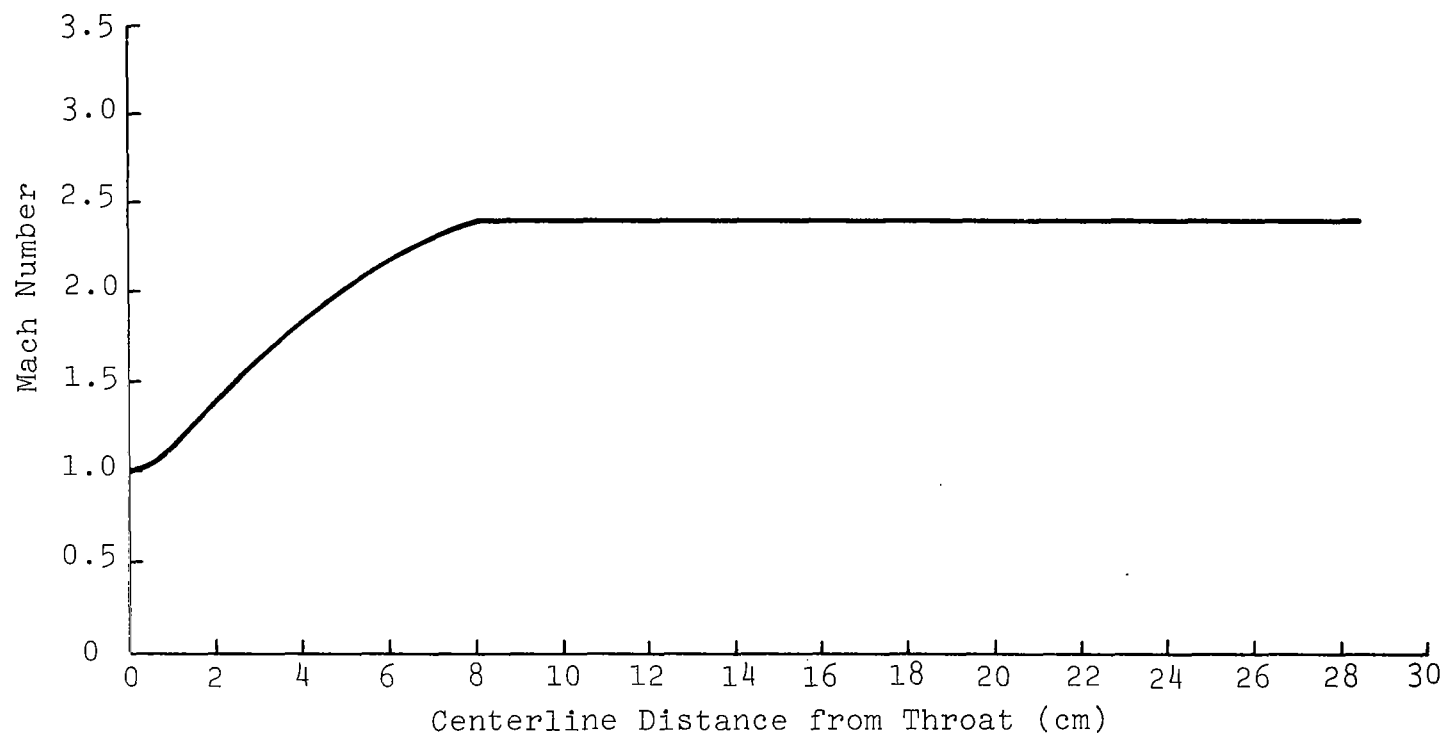


Fig. 3 Detonation Tube 1/8-Scale, Combustor Nozzle Centerline Mach Number Distribution

$$\phi = 1.0, \alpha + \beta = 4^\circ, P_5 = 8.309 \times 10^5 \text{ N/m}^2, H_5 = 578.4 \frac{\text{cal}}{\text{gm}}$$

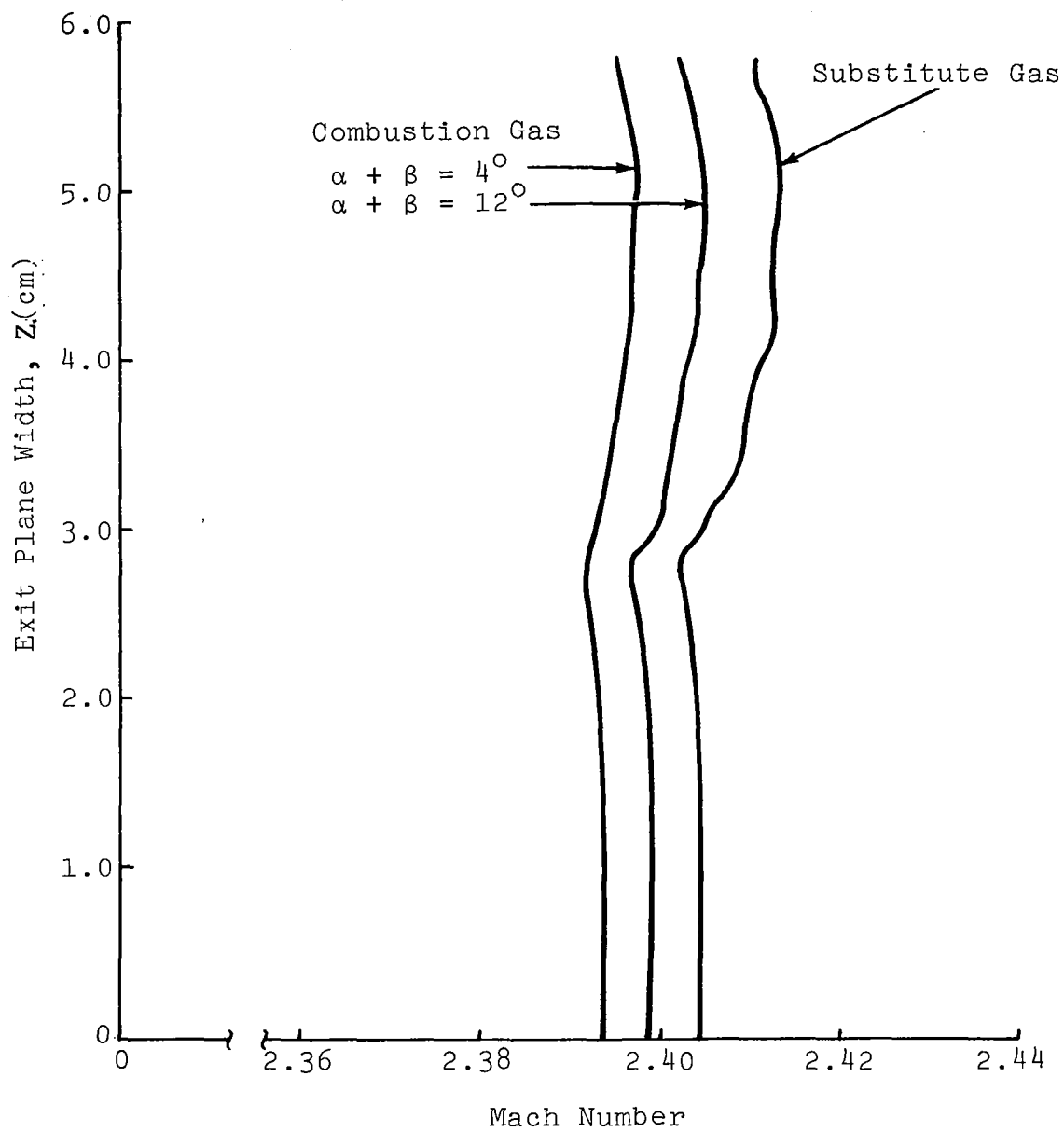


Fig. 4 Combustor Nozzle Exit Plane Mach Number Distribution

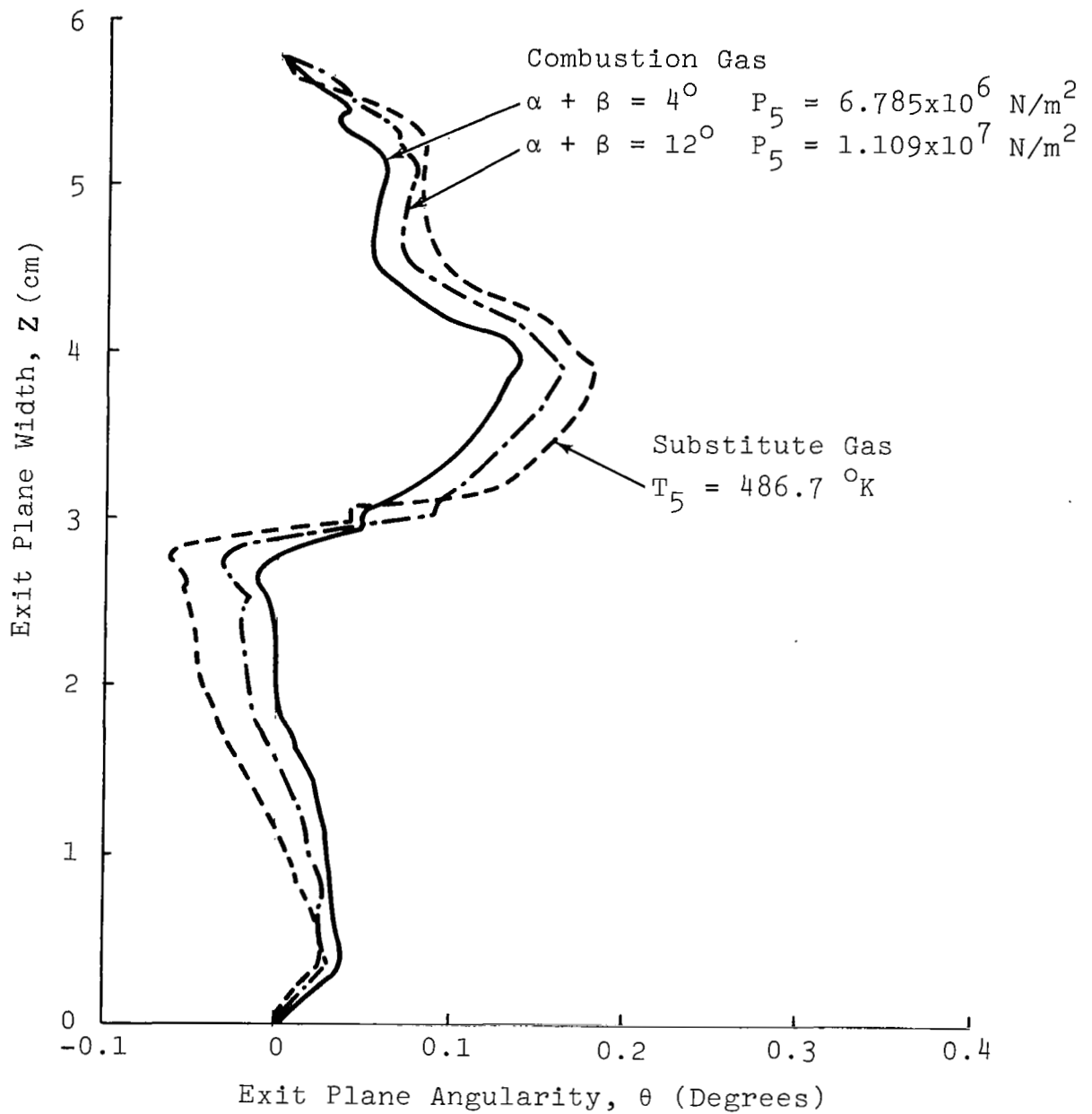


Fig. 5 Detonation Tube Contoured Nozzle Exit Plane Flow Angularity

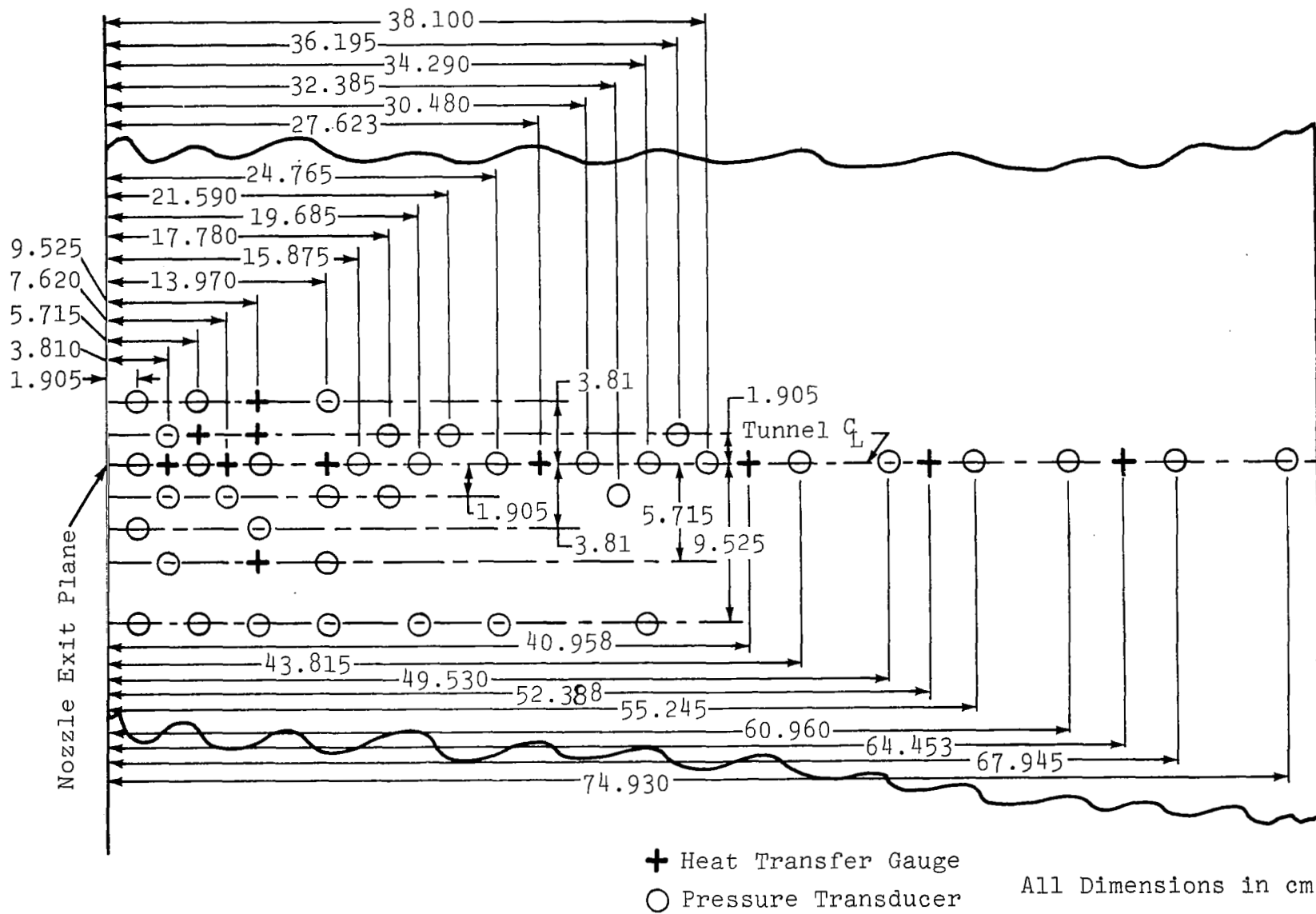


Fig. 6 Gauge Locations - Afterbody Model



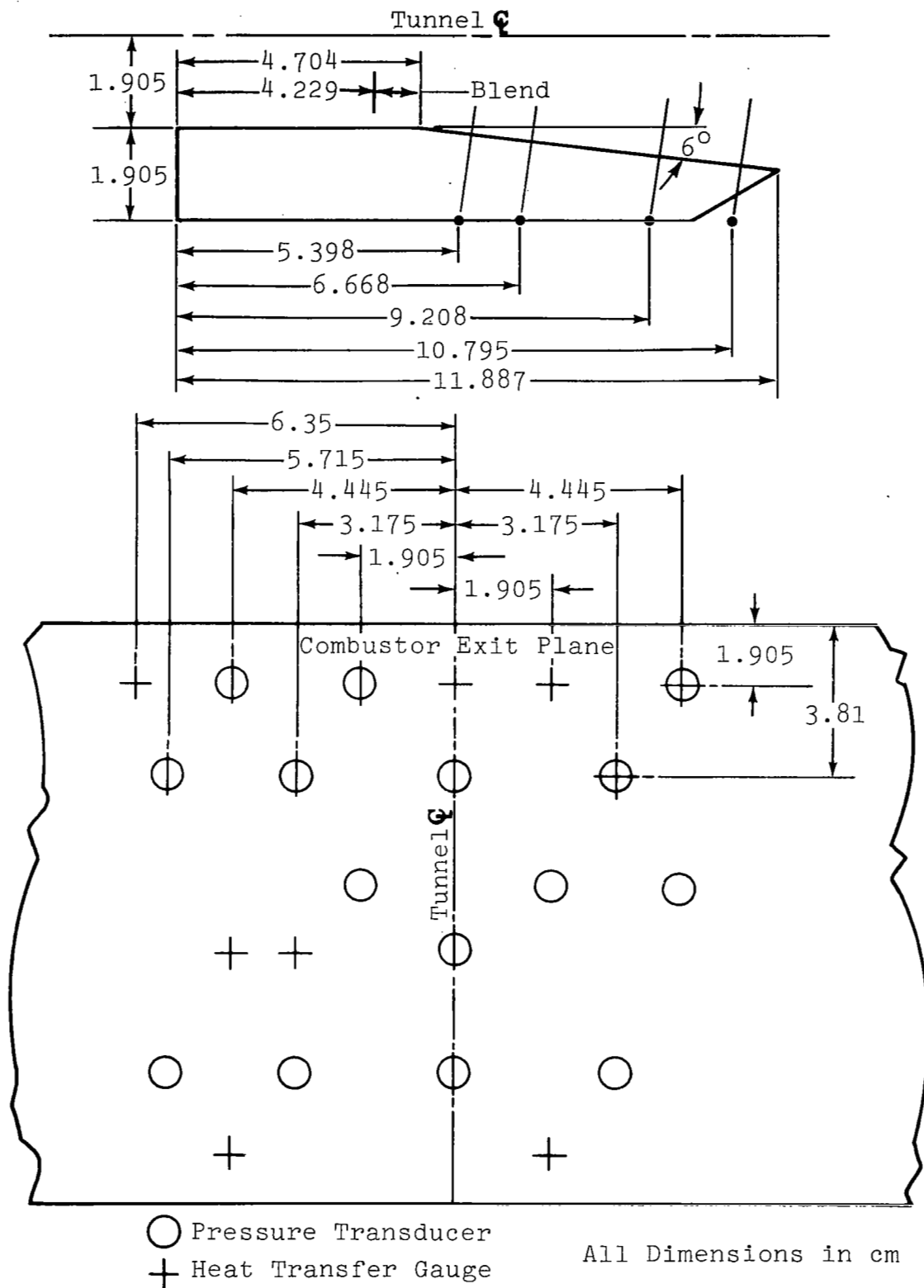


Fig. 7 Cross-Section and Gauge Locations-Cowl Model

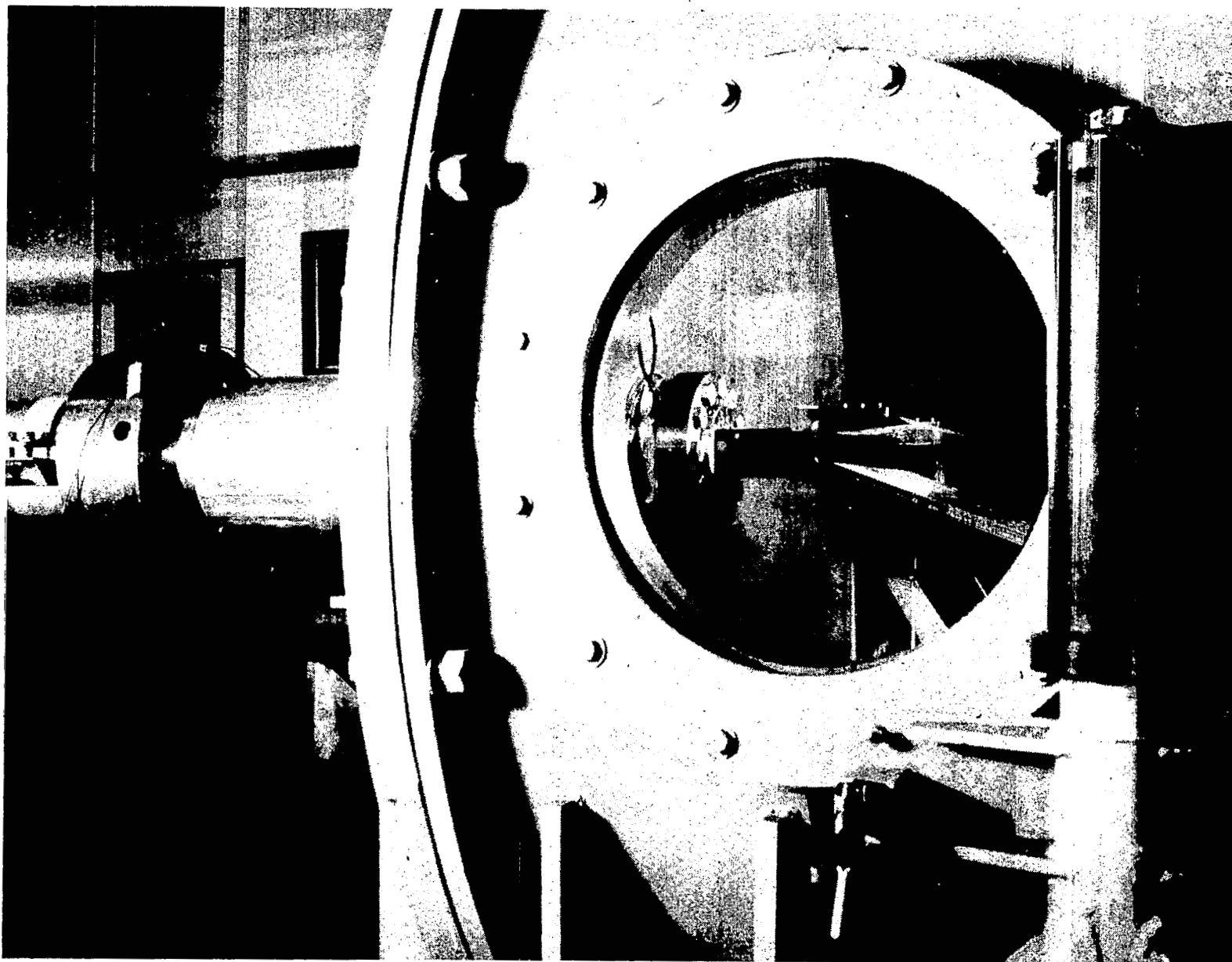


Fig. 8 Photograph of Model Mounted in Test Section

graph of the cowl and afterbody mounted in the test section of the simulator.

For part of the experiments two different sets of extensions to the nozzle side walls were employed. In one case the walls were extended to the trailing edge of the cowl (11.887 cm) and in the second the extensions were three times this length (33.661 cm). Photographs of the model with these extensions are shown in Figs. 9 and 10, respectively.

### Instrumentation

Tunnel operating conditions for this program were monitored with piezoelectric transducers, Kistler models 603L and 607. Calibrations were checked with a deadweight tester and ranges and accuracies are given in Table 2. Other measurement equipments are listed in Table 3.

Model pressures were measured over three ranges with semiconductor strain gauge transducers (Kuhlite mod VQH-250-5 for  $0 - 3.45 \times 10^4 \text{ N/m}^2$ , mod VQI-250-20 for  $0 - 1.38 \times 10^5 \text{ N/m}^2$ , and mod VQS-250-200 for  $0 - 1.38 \times 10^6 \text{ N/m}^2$ ). These gauges were calibrated statically against a manometer and dynamically in a 3.81 cm ( $1\frac{1}{2}$ -in.) ID shock tube. The static calibration showed excellent linearity (Fig. 11) with an accuracy (combined linearity and repeatability) of  $\pm 0.2$  percent. The dynamic calibration showed agreement with the static calibration within the error limits of the recording instruments and shock tube accuracy (better than  $\pm 2$  percent). The pressure transducers have a first diaphragm resonance at 70 kHz and were filtered to 5 kHz to remove any diaphragm and/or tunnel "ringing" while preserving a 70  $\mu\text{sec}$  rise time which yields a good dynamic response within the 3 msec test time.

Heat transfer rates were measured, where possible, with thin film heat transfer gauges (Ref. 7) to an accuracy of  $\pm 7$  percent. The heat transfer gauges consist of a thin platinum film on a pyrex substrate. We assume that the substrate is a one dimensional semi-infinite slab and from measurements of the slab surface temperature versus time we compute the local heating rates using analog circuits.

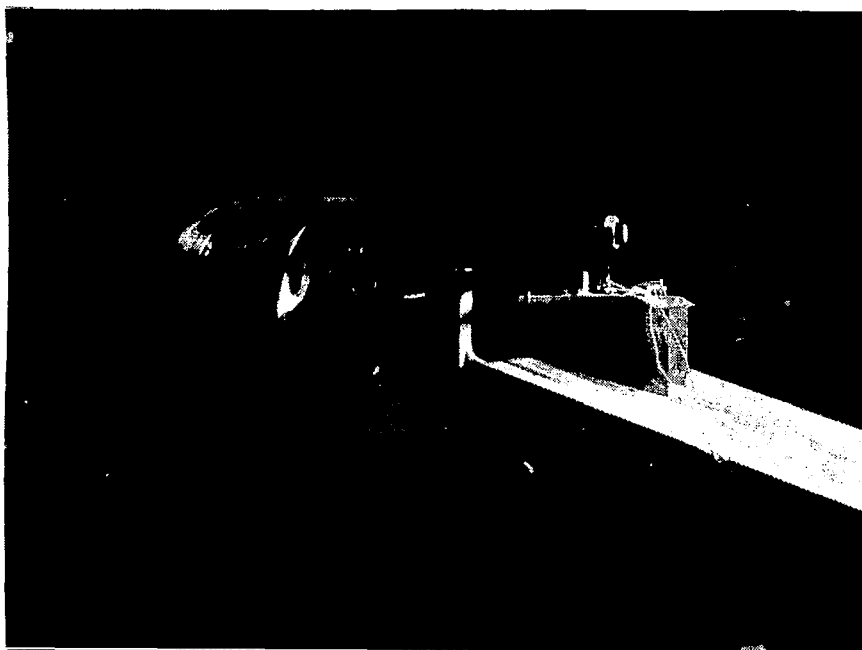


Fig. 9 Model with Short Side Plates

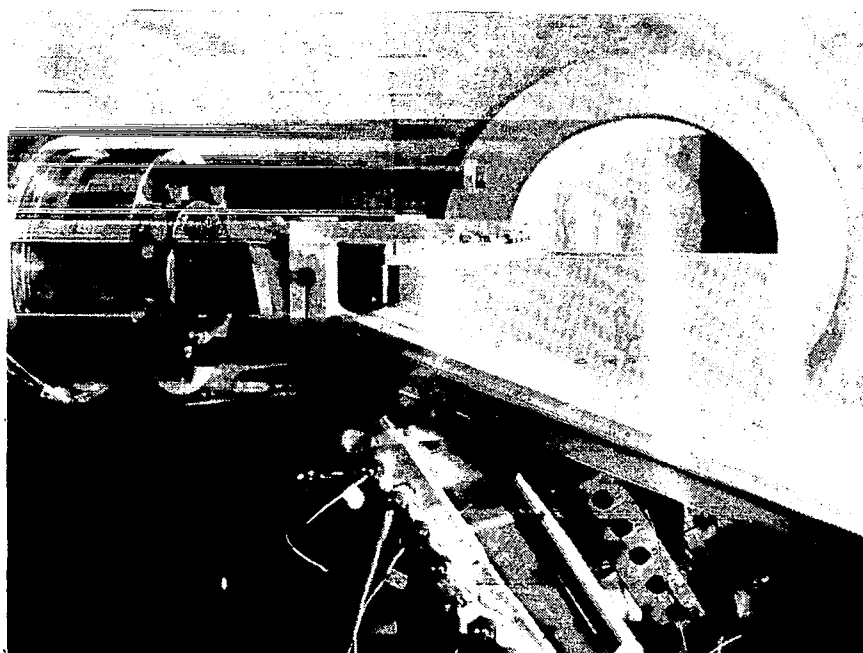


Fig. 10 Model with Long Side Plates

TABLE 2 MEASUREMENT ACCURACY

Tunnel Parameter		Accuracy*	Range
$P_1$	Tunnel Driven Initial Pressure	$\pm 689 \text{ N/m}^2$	$0 \rightarrow 6.89 \times 10^5 \text{ N/m}^2$
$P_4$	Tunnel Driver Initial Pressure	$\pm 1.38 \times 10^5 \text{ N/m}^2$	$0 \rightarrow 1.38 \times 10^7 \text{ N/m}^2$
$P_5$	Stagnation Pressure	$\pm 3.10 \times 10^5 \text{ N/m}^2$	$0 \rightarrow 1.38 \times 10^7 \text{ N/m}^2$
$U_{\text{inc}}$	Incident Wave Speed	$\pm 30 \text{ m/sec}$	$0 \rightarrow 900 \text{ m/sec}$
$P_{T2}$	Impact Pressure	$\pm 6.89 \times 10^4 \text{ N/m}^2$	$0 \rightarrow 6.89 \times 10^6 \text{ N/m}^2$
$\dot{Q}$	Heat Transfer Rate	$\pm 7\%$	$0 \rightarrow 50 \text{ gm cal/cm}^2\text{sec}$

TABLE 3 INSTRUMENTATION AND DATA RECORDING EQUIPMENT

Pressure Transducers		
Manufacturer	Model No.	Max Range
Kuhlite	VQS-250-200	$1.38 \times 10^6 \text{ N/m}^2$
Kuhlite	VQL-250-20	$1.38 \times 10^5 \text{ N/m}^2$
Kuhlite	VQH-250-5	$3.45 \times 10^4 \text{ N/m}^2$
Kistler	603 L	$1.03 \times 10^7 \text{ N/m}^2$
Kistler	607	$4.13 \times 10^8 \text{ N/m}^2$
Data Recording and Reduction		
Honeywell	7600 tape recorder	1.5 MHz bandwidth
D.C.S.	Gov-3, VCO's	$\pm 2\text{v}$ , $\pm 32 \text{ kHz}$
D.C.S.	GMA-5, line drivers	—
D.C.S.	GFD-14, discriminators	$\pm 10\text{v}$ , $\pm 16 \text{ kHz}$
Hewlett-Packard	A/D converter	12 bit, $50 \mu\text{sec/word}$
Hewlett-Packard	21 MX computer	—
Texas Instruments	700 ASR terminal and cassette tape drive	

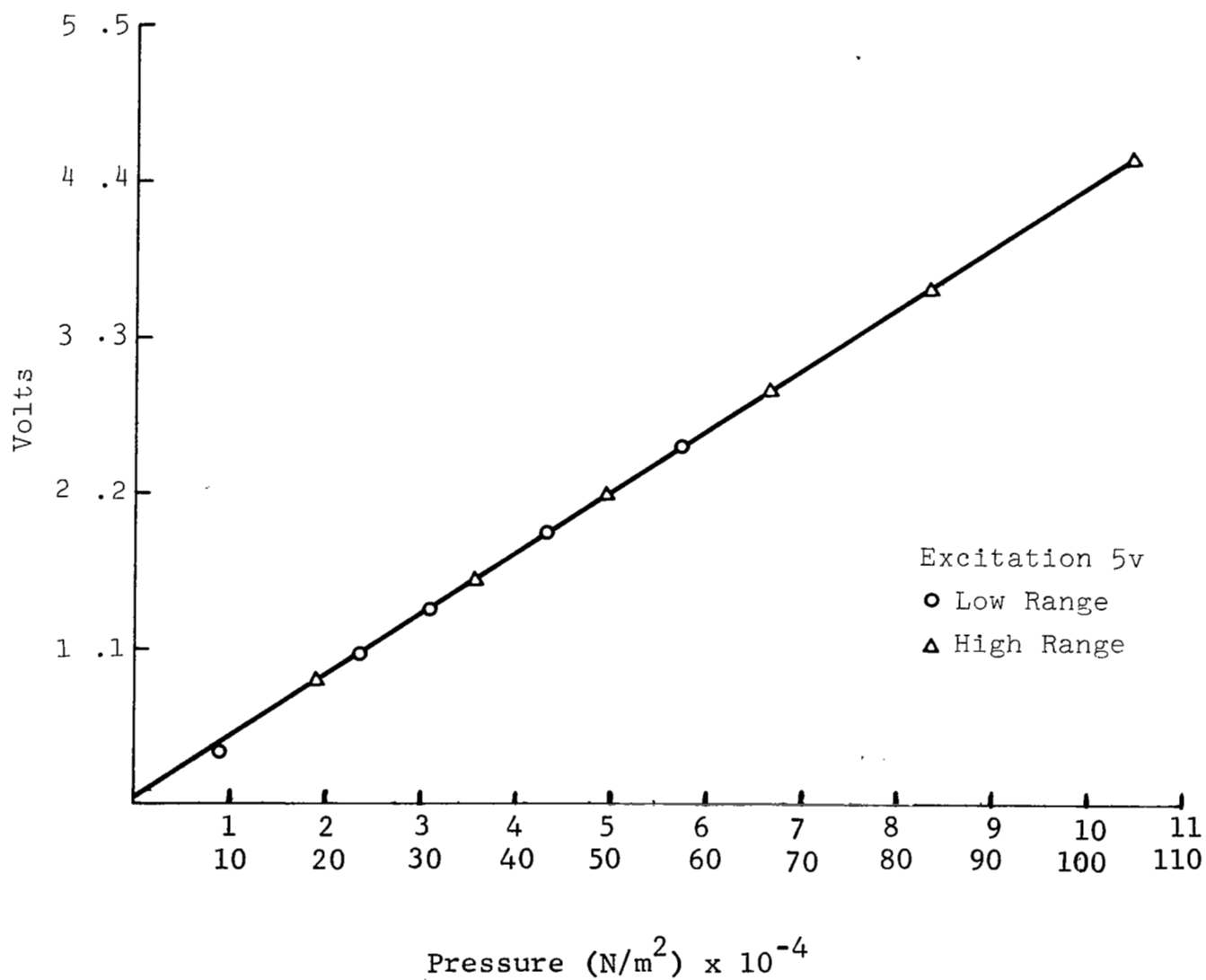


Fig. 11 Static Calibration of  $1.38 \times 10^5 \text{ N/m}^2$  Pressure Transducer No. 3-8

## Data Acquisition and Reduction

The data, after suitable signal conditioning, were recorded on a 35-channel FM multiplex tape system and played back one channel at a time for reduction. Preliminary data reduction was performed by oscilloscope and camera; however, at mid-program time a mini-computer and 12-bit A/D converter were made available. The computer was used to reduce all subsequent data and reduce much of the previous data tapes.

The system signal-to-noise ratio, S/N, was 40 db in the worst case. There was, however, noise from the combustion process in addition to the -40 db of electronic noise. This noise is noted in Fig. 12 which is a typical pressure trace obtained during runs with combustion products. When we assume that this noise is uncorrelated with the data, then averaging a significant number of samples leads to an improvement in S/N. The computer reduction system, the most accurate component in the measuring system, has a 50  $\mu$ sec/word throughput rate which is sufficient to reconstruct an analog signal of 10 kHz. Our data were averaged over the 3 msec test time resulting in an increase in S/N of 7.75/1 or 18 db (i.e.,  $\sqrt{60}$  where 60 is the number of samples taken during the test time).

The signal conditioning, recording, and reduction systems were calibrated by injecting known square waves (1 percent) at the transducer and reducing these as if they were data. When we combine the electronic noise, combustion noise, transducer inaccuracy, and recording and reduction system inaccuracy with the random variation in tunnel performance, we have a 3 percent mean error for the combustion runs and 2 percent mean error for the substitute gas runs. The bulk of these errors are caused by variations in tunnel performance and/or combustion noise since all other contributions are 1 percent or less.

## Flow Visualization

Several attempts were made at obtaining glow photographs on combustion runs. The very high light levels associated with the combustion processes gave us very low contrast on these photos. Apparently, the light from the stagnation region, shining through the large nozzle throat, reflects on the stainless steel vacuum chamber walls and scatters throughout the flow, completely overwhelming any variations in light emanating from the flow. The



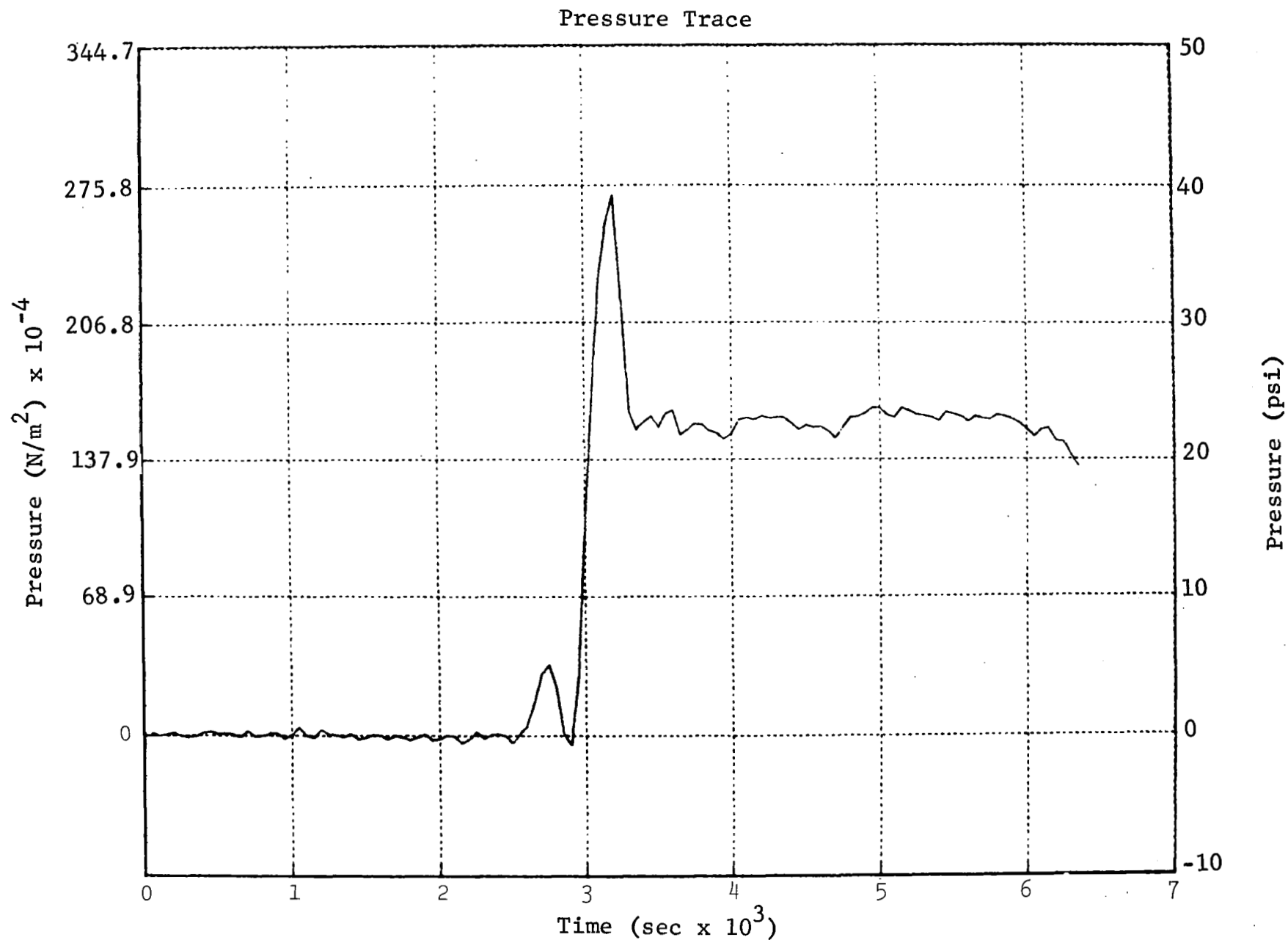


Fig. 12 Pressure Trace for Run with Combustion Products Indicating Increased Noise Due to Flow (each vertical division = 10 psi)

light levels were so high that a 100:1 neutral density filter had to be used with even the slowest film. A rough look at the flow with a spectrograph showed less intensity in the 5600Å region, so we tried interference filters to take photos in that spectral region. Unfortunately, light from downstream stagnation areas has roughly the same spectrum as the upstream stagnation area and the low contrast problem was repeated at a lower light level.

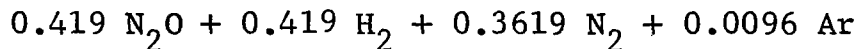
Schlieren photos were not attempted since the light levels would "wash out" our white spark source. If a pulsed laser of the right wavelength were available it might be possible to obtain schlieren photos with filtering.

### 3. DETONATION TUBE RUNNING CONDITIONS

#### Combustion Gas ( $\phi = 1.0$ )

A complete description of the operation, performance, and computational procedures involved in determining the detonation tube simulator running conditions is given in Ref. 1. As discussed earlier, all the combustion gas data presented herein were obtained using the backward-running detonation technique.

There are any number of gas mixtures we could have used for the simulation (Ref. 1). The particular one we chose was



which would give us the ideal stagnation enthalpy at an incident shock Mach number of 2.5. In practice, we developed reliable and reproducible running conditions at an incident shock Mach number of 2.16 which meant the stagnation enthalpy was about 36 cal/gm lower than ideal. The absolute total enthalpy of the flow is many thousands of cal/gm and this small decrement in total enthalpy produced insignificant changes in other thermodynamic and transport properties of the gas.<sup>2</sup> The measured stagnation pressure,  $P_5$ , was  $1.0688 \times 10^7 \text{ N/m}^2$  (1550 psia). Typical stagnation pressure oscilloscope records are shown in Fig. 13a and illustrate the constant pressure level obtained for about 3 milliseconds.

The measured static pressure at the exit of the nozzle,  $P_3$ , and on the flat portion of the cowl (before the 6 degree bend) was  $7.033 \times 10^5 \text{ N/m}^2$  (102.0 psia). An oscilloscope picture showing this measurement is presented in Fig. 13b. Based on the measured  $P_5/P_3$  ratio, the ideal total enthalpy, and assuming an isentropic, equilibrium expansion, we computed (Ref. 5) the exit plane Mach number to be 2.37. Table 4 below presents the significant running conditions obtained by the procedure outlined previously and used for our data reduction and afterbody flow field predictions.

#### Substitute Gas

The detonation tube facility was operated in the reflected shock tube or shock tunnel mode (Ref. 1) in order to generate the

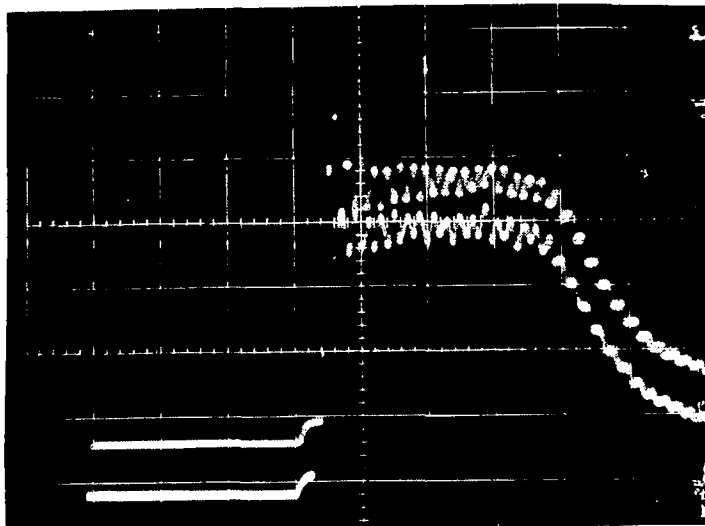


Fig. 13a Oscilloscope Record of Detonation Tube Stagnation Pressure,  $P_5$  (Two Independent Transducers). Both Beams Horizontal Sweep: 1 msec/cm. Both Beams Vertical Deflection:  $2.61 \times 10^6$  N/m<sup>2</sup>/cm. Combustion Gas Run.

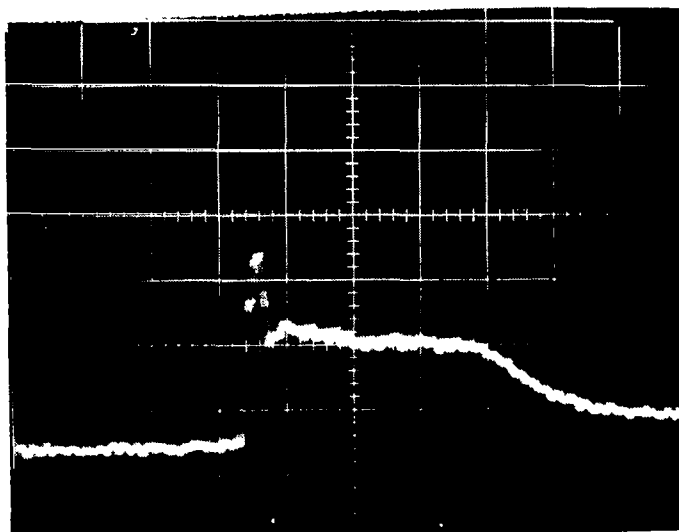


Fig. 13b Oscilloscope Record of Combustor Nozzle Exit Plane Static Pressure,  $P_3$ . Horizontal Sweep: 1 msec/cm. Vertical Deflection:  $4.41 \times 10^5$  N/m<sup>2</sup>/cm. Combustion Gas Run.

TABLE 4 COMBUSTION GAS RUNNING CONDITIONS

$$\phi = 1.0, \alpha + \beta = 12^\circ, \frac{1}{8} \text{ Scale}$$

	Ideal (Ref. 1)	Based on Measured $P_5/P_3$
$P_5$ (N/m <sup>2</sup> )	$1.109 \times 10^7$	$1.0688 \times 10^7$
$H_5$ (cal/gm)	578.4	578.4
$T_5$ (°K)	3409	3406
$P_3$ (N/m <sup>2</sup> )	$8.18 \times 10^5$	$7.033 \times 10^5$
$T_3$ (°K)	2368.0	2323.0
$M_3$	2.311	2.371
$\gamma_3$	1.2051	1.2081
Rey. No. <sub>3</sub> (m <sup>-1</sup> )	$3.081 \times 10^7$	$2.786 \times 10^7$

required stagnation conditions for the substitute gas runs. The substitute gas mixture chosen was 58 percent Freon 13B1 and 42 percent Argon at a stagnation temperature of 486°K (see Ref. 1 for a discussion on the selection of substitute gas candidates). The incident shock wave strength required to produce that stagnation temperature was computed from ideal gas shock tube equations using an average value of  $\gamma$  across the incident and reflected shock waves. The thermodynamic properties of this particular substitute gas were computed using the procedure developed in Appendix A and are given in Table A-1. To achieve full scale Reynolds number in our  $\frac{1}{8}$  scale tests we required a stagnation pressure of  $4.10 \times 10^5$  N/m<sup>2</sup> (59.5 psia).

We developed a repeatable running condition in our detonation tube facility with this substitute gas mixture which gave us a measured stagnation pressure of  $4.41 \times 10^5$  N/m<sup>2</sup> (64 psia) and a

calculated stagnation temperature of  $464^{\circ}\text{K}$ . The design of our facility is such that it is mechanically difficult to run at pressures as low as this. Therefore, we did not feel it was warranted to spend time refining the running conditions further.

Another problem we encountered in making reflected shock tube runs in substitute gas mixtures was the slow jump in pressure from the pressure level behind the incident wave to the pressure level behind the reflected shock wave. Typical substitute gas stagnation pressure records are shown in Fig. 14a and illustrate the point. The basic problem is that as the reflected shock wave propagates back through the boundary layer behind the incident wave, the reflected shock tends to bifurcate, i.e., develop a Mach stem configuration, rather than stay normal to the wall (Ref. 8). Thus, part of the gas behind the reflected shock is processed by two oblique shock waves, instead of by a normal shock wave as ideal theory assumes. The lower the  $\gamma$  of the gas, the worse the bifurcation becomes. The substitute gas mixtures we are concerned with have extremely low  $\gamma$ 's (less than 1.2). This bifurcation phenomena introduces some uncertainty in the state of the gas behind the reflected shock and was another reason we did not attempt to refine the substitute gas running conditions. It should be pointed out, however, that in a steady flow wind tunnel test where the substitute gas will be drawn directly from some sort of high pressure storage reservoir, the bifurcation problem will not exist and the substitute gas properties will be accurately known.

For these substitute gas runs the static pressure at the exit of the nozzle and on the flat portion of the cowl,  $P_3$ , measured  $2.76 \times 10^4 \text{ N/m}^2$  (4.0 psia). From the measured  $P_5/P_3$  ratio and the calculation procedure described earlier, we determined the Mach number at the exit plane of the nozzle to be 2.4. This agrees very well with the value of 2.42 calculated for our nozzle using the two dimensional M-O-C program (Ref. 5).

Figure 14b shows a typical cowl static pressure measurement. Note the slow rise ( $\approx 1 \text{ msec}$ ) to the final pressure level, similar to that of the stagnation pressure records, Fig. 14a.

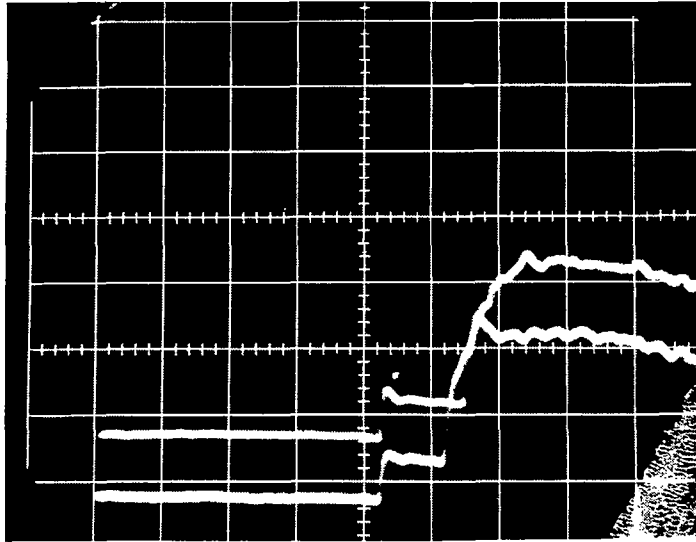


Fig. 14a Oscilloscope Record of Substitute Gas Reflected Shock Stagnation Pressure,  $P_5$  (Two Independent Transducers). Both Beams Horizontal Sweep: 1 msec/cm. Both Beams Vertical Deflection:  $1.77 \times 10^5 \text{ N/m}^2/\text{cm}$ .

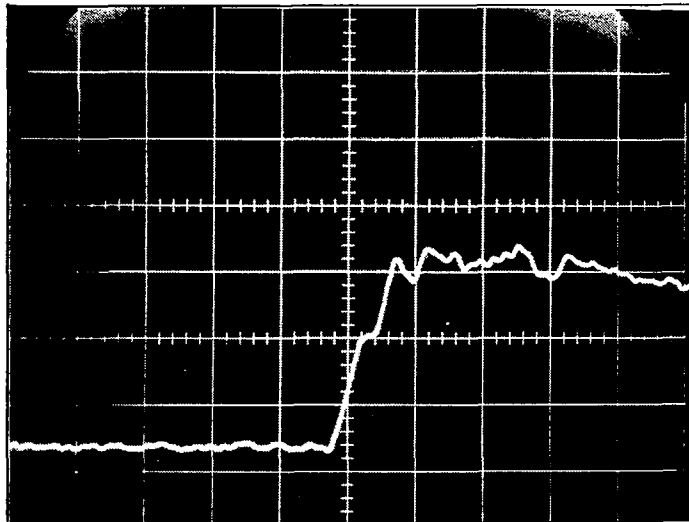


Fig. 14b Oscilloscope Record of Combustor Nozzle Exit Plane Static Pressure,  $P_3$ . Horizontal Sweep: 1 msec/cm. Vertical Deflection:  $9.86 \times 10^3 \text{ N/m}^2/\text{cm}$ . Substitute Gas Run.

#### 4. AFTERBODY FLOW FIELD PREDICTIONS

Analysis of the experimental results involved a continuing effort to take into account all of the nonidealities in the flow and nozzle geometry. This section explains the many afterbody flow field calculations carried out during the course of the program.

For the calculations presented all combustion gas thermodynamic data were derived from the computer program of Ref. 4. Substitute gas thermodynamic data were generated by a new procedure, described in Appendix A of this report, rather than by the procedure given in the appendix of Ref. 1. We found the new procedure to be considerably more accurate. The flow fields including the presence of shock waves, were calculated using the two dimensional, method-of-characteristics program of Ref. 5. The baseline geometry of the afterbody and cowl surfaces was the same as given in Ref. 1. The coordinate system is shown in Fig. 17.

##### Afterbody

$$\bar{Y} = 0.7187 \bar{X}^2 + 1.0$$

$$0 \leq \bar{X} \leq 0.25$$

$$Y = 0.35935 \bar{X} + 0.95508$$

$$0.25 \leq \bar{X} \leq 18.54$$

##### Cowl

$$\bar{Y} = 0$$

$$0 \leq \bar{X} \leq 1.11$$

$$\bar{Y} = -0.4204 \bar{X}^2 + 0.933 \bar{X} - 0.518$$

$$1.11 \leq \bar{X} \leq 1.235$$

$$\bar{Y} = -0.1051 \bar{X} + 0.1232$$

$$1.235 \leq \bar{X} \leq 3.12$$

where  $\bar{Y} = Y/Y_3$ ,  $\bar{X} = X/Y_3$ , and  $Y_3$  is the height of the combustor exit.

As a result of these calculations we found that the basic afterbody flow field and its pressure distribution were relatively insensitive to small changes in combustion gas thermodynamic properties and combustor exit Mach number. However, small changes in the model geometry and three dimensional side expansion effects caused major perturbations in the flow field and pressure distributions.

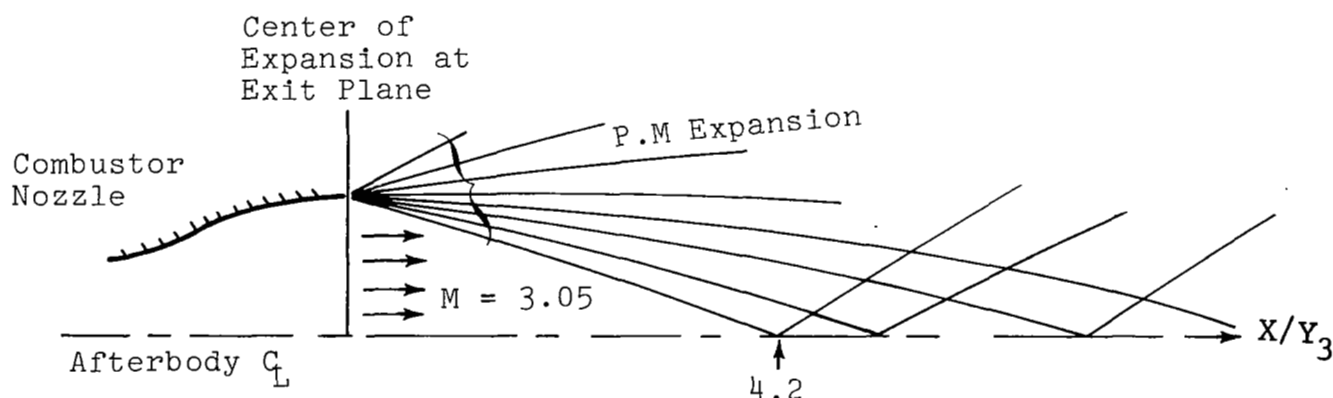


The first point is illustrated in Fig. 15. Here we show calculated, two dimensional pressure distributions for the basic model geometry for three slightly different combustion gas conditions.

Distribution A is the ideal,  $\frac{1}{8}$  scale,  $M_\infty = 8$ ,  $\alpha + \beta = 12^\circ$ , case presented in Fig. 14 in Ref. 1. Distribution B is for the ideal flow generated by the detonation tube/combustor nozzle we actually used assuming the ideal stagnation conditions of Distribution A. Distribution C is for the experimental flow conditions as determined from our measurements of the detonation tube stagnation pressure ( $P_5$ ) and combustor nozzle exit plane static pressure ( $P_3$ ).

### Side Expansion (Three Dimensional) Effects

To provide a closer comparison with the actual flow, we estimated the effects of the flow expansion around the side walls on the centerline pressure distribution. The two dimensional Mach number on the afterbody surface was 3.05 after the 19.76 degree turn at the exit plane. We assumed a Prandtl-Meyer expansion starting at the side edge of the nozzle and propagating through a uniform flow at that Mach number (see sketch as viewed normal to the afterbody surface). Careful examination of the Mach cones at



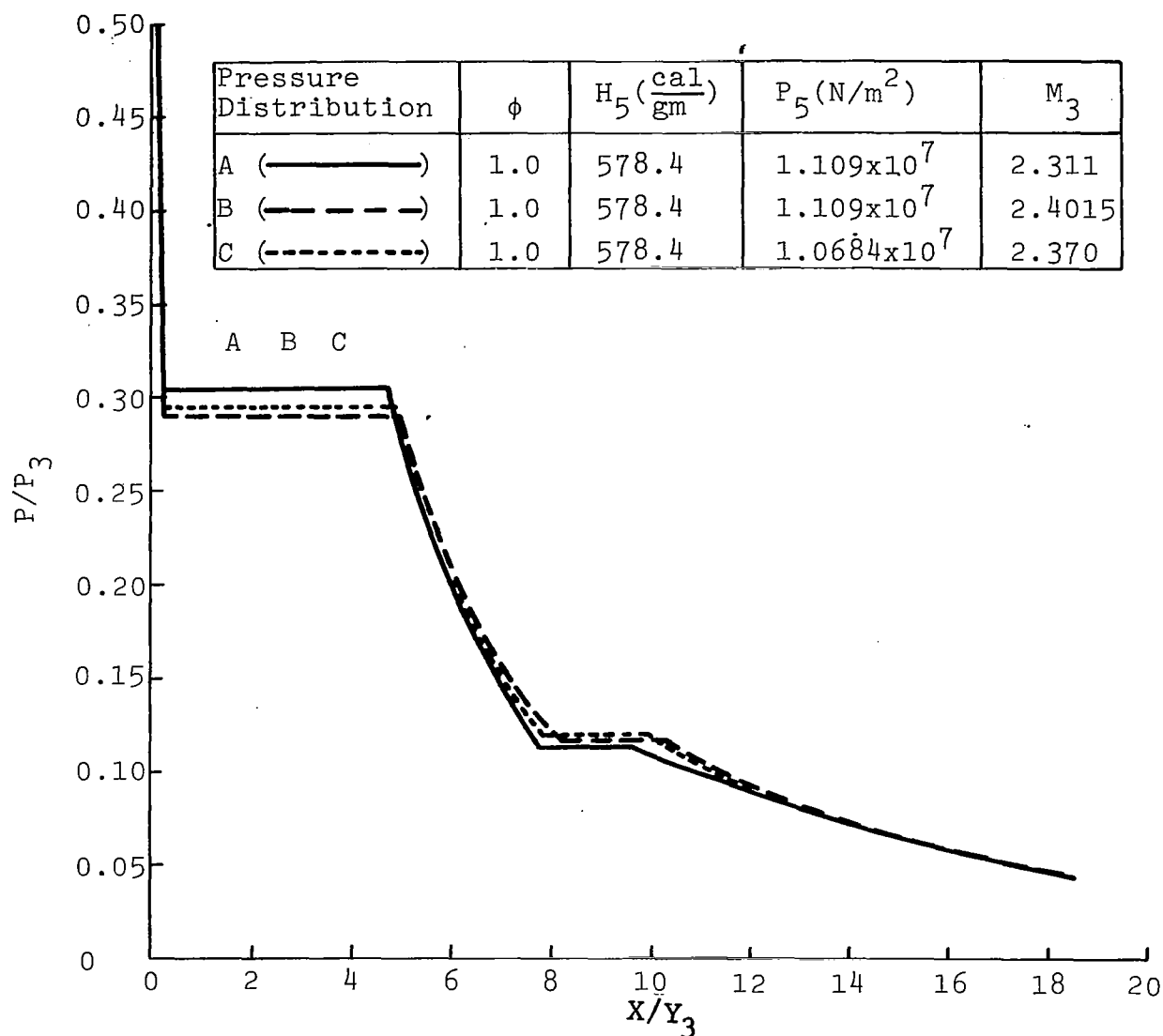
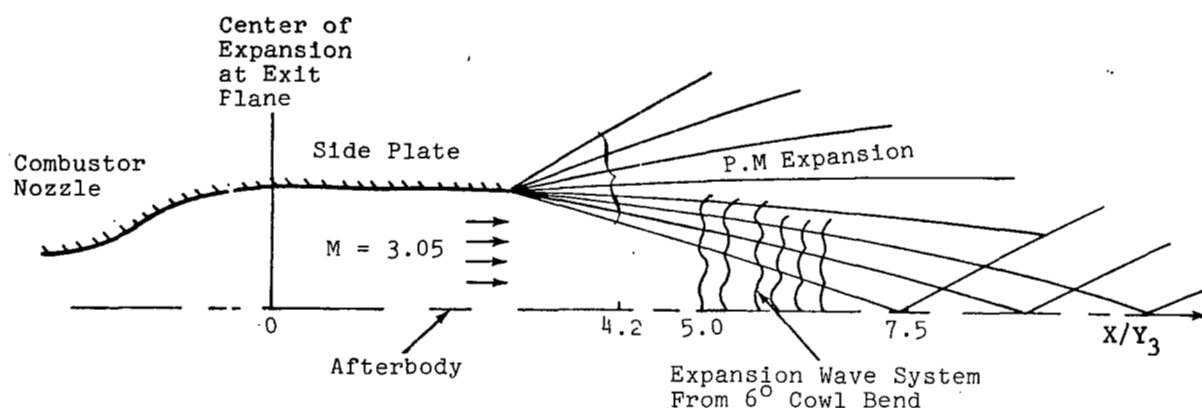


Fig. 15 Theoretical, Two Dimensional, Afterbody Pressure Distributions

1/8-scale,  $M_\infty = 8$ ,  $\alpha + \beta = 12^\circ$

the combustor exit showed that for this case the flow on the surface was locally two dimensional. Using the two dimensional M-O-C program (Ref. 5) we calculated the pressure distribution along the afterbody centerline, normalized this by the undisturbed static pressure at  $M = 3.05$ , and used this normalized pressure ratio as a correction factor to the two dimensional pressure distribution. Figure 16 shows a typical two dimensional pressure distribution corrected for this three dimensional side expansion effect.

As the test program proceeded we tried to enlarge the region of two dimensional flow by putting straight sideplates on the combustor nozzle, thus delaying the side expansion effect until further downstream (see sketch below).



We used the same calculation procedure as described above and determined a three dimensional pressure ratio correction factor for the nozzle with the extended sideplates. The results of this calculation are also shown in Fig. 16. Note that in this case the expansion wave system from the 6 degree bend in the cowl impinges on the afterbody at about  $X/Y_3 = 5.0$ , before the side expansion wave system on the afterbody reaches the centerline. This means that the side expansion wave Mach lines should be slightly curved aft of  $X/Y_3 = 5.0$ , and will cross the centerline a little further downstream. We did not take this effect into account, and assumed all the characteristics were straight. In the no-side-plate case we also neglected the region  $0 < X/Y_3 < 0.25$ , where

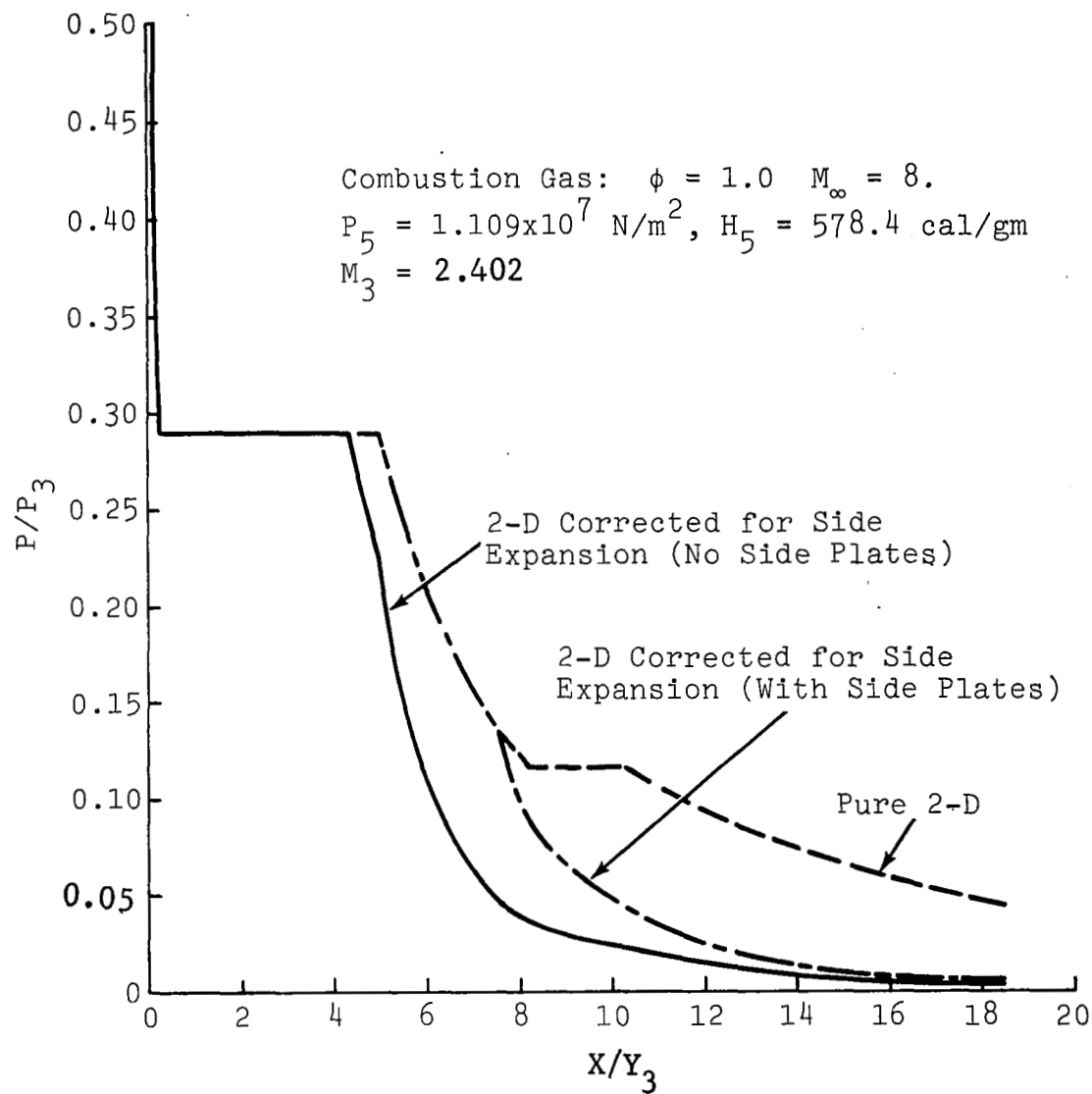


Fig. 16 Typical Two Dimensional Afterbody Pressure Distribution on the Centerline Corrected for Nozzle Side Expansion Effects

the flow accelerates from  $M_3 \approx 2.4$  to  $M = 3.05$  as it goes around the 19.76 degree afterbody bend.

Note that no side expansion correction has to be applied to the cowl centerline pressure distribution. The length of the cowl is such that the leading side expansion characteristic does not reach the centerline until  $X/Y_3 \approx 4.2$ .

### Model Geometry Effects

As discussed in the section on experimental pressure distributions (refer to Section 5), the first test runs were made with a configuration that had rearward facing steps of about 0.8 mm in height at the nozzle/model junctions. These steps arose through the initial requirement to isolate the model from shock tube recoil. Using the two dimensional M-O-C program (Ref. 5) and assuming various size and various angle ramps at the junctions, we were able to calculate pressure distributions that very closely resembled the measured ones. (This program stops running if a subsonic Mach number is encountered so we could not assume square steps.) We were able to show that if a certain strength shock wave were generated in the uniform flow at the combustor exit/afterbody junction, it would propagate across the flow field and intersect the cowl at  $1.5 < X/Y_3 < 2$ . The shock wave would then reflect back through the flow field and impinge on the afterbody at  $X/Y_3 \approx 7$ . We immediately redesigned the models to eliminate all steps, sacrificing the recoil isolation that had been shown to be unnecessary.

The afterbody pressure distributions from the redesigned models still had some unexpected disturbances in them. We noticed that there seemed to be a slight flare about one cm wide on the upper surface of the nozzle at the exit plane. The flare had about a two degree slope. We used the two dimensional M-O-C program to calculate a flow field with this geometry. Figure 17 is a scale, characteristics drawing showing all the wave systems of interest. Figure 18 shows the corresponding pressure distribution on the afterbody surface. Note that the Prandtl-Meyer expansion from just a two degree expansion produces a 22 percent surface pressure drop between  $3.0 < X/Y_3 < 3.5$  and that the shock wave from the two degree recompression brings the pressure back to its original value. Experimental results showing this same effect at the same location are presented in the next section.

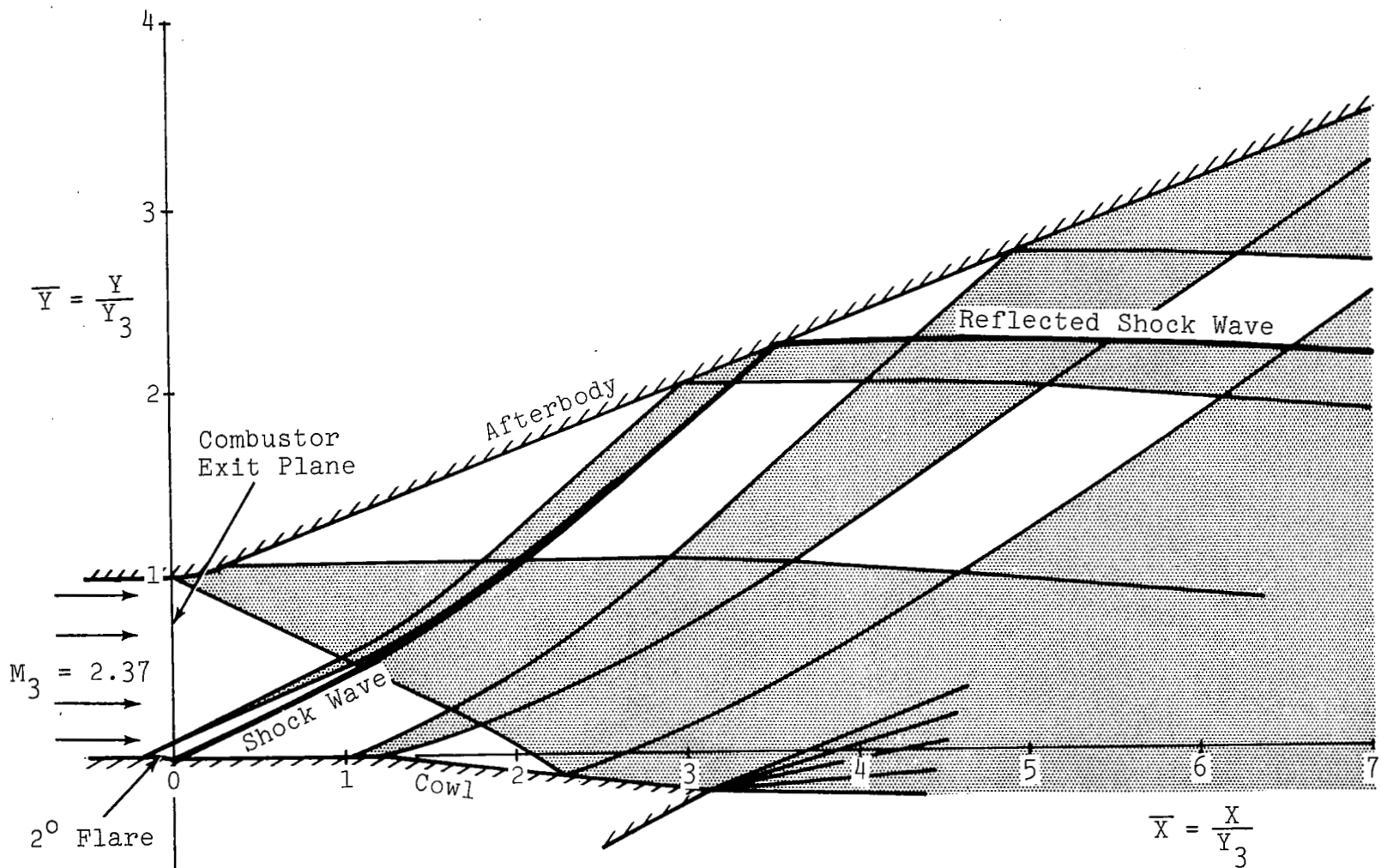


Fig. 17 Characteristics Drawing Showing Expansion and Shock Wave from 2-deg Flare at Combustor Exit

$$\phi = 1.0, \alpha + \beta = 12 \text{ deg}, P_5 = 1.0684 \times 10^7 \text{ N/m}^2, H_5 = 578.4 \frac{\text{cal}}{\text{gm}}$$

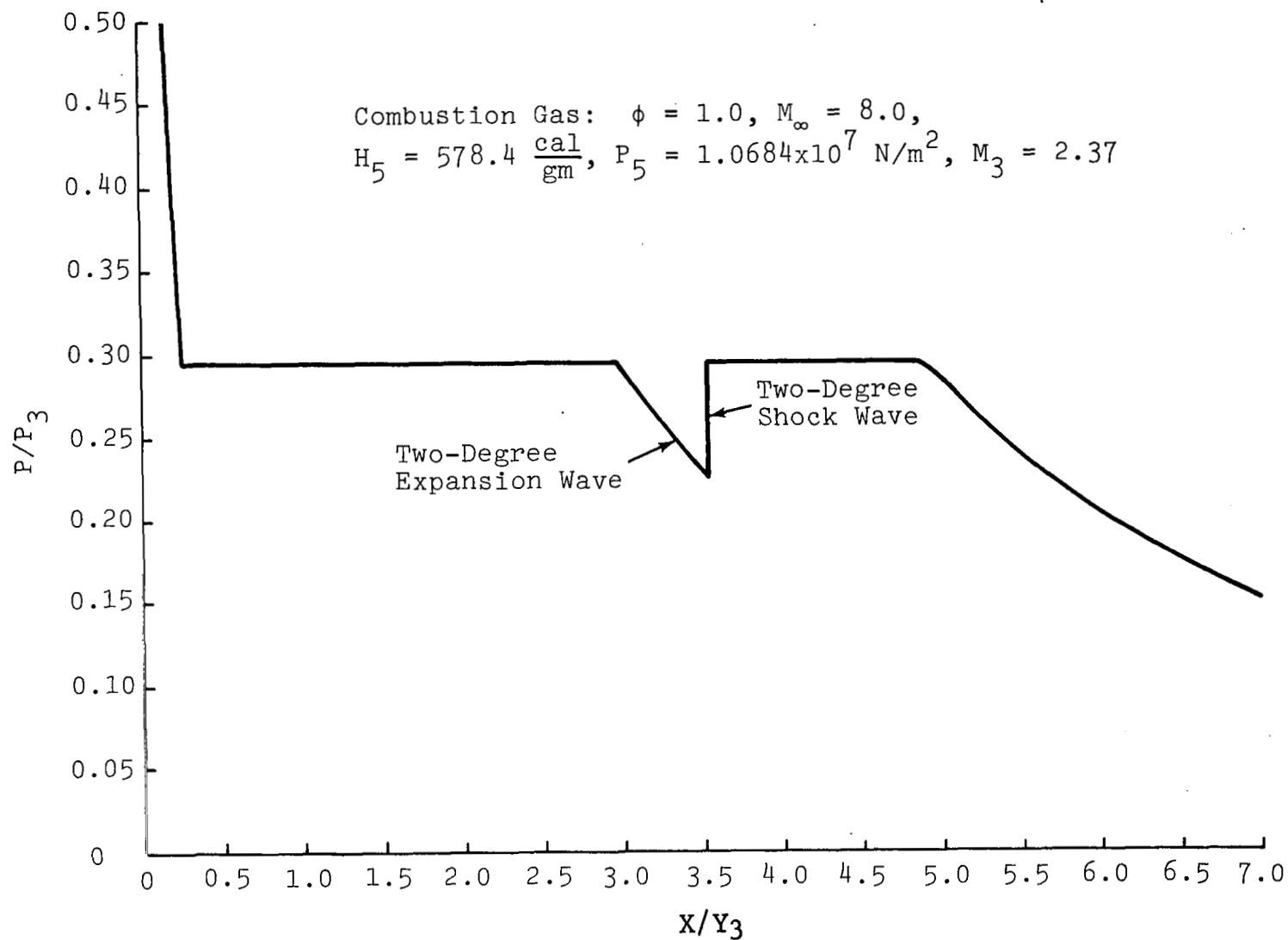


Fig. 18 Afterbody Surface Pressure Distribution Showing Pressure Perturbation Due to a Two-Degree Expansion and Re-Compression

The important thing we learned from all these calculations is that seemingly minor blemishes on model surfaces can cause major perturbations on opposite wall pressure distributions and will do so on the full scale vehicle. For example, a two degree Prandtl-Meyer expansion causes an 11 percent static pressure drop in the free stream. But when such an expansion reflects from a solid surface, the surface pressure drop is double that amount.



## 5. EXPERIMENTAL RESULTS

### Pressure Distributions

The goal of this program is to validate that detonation tube products and substitute gases will duplicate the pressure distributions from the actual engine exhaust on the afterbody/cowl portion of the vehicle. We concentrated first, therefore, on obtaining good data from the simulated combustion products. These data at first contained several anomalies that required understanding prior to attempting substitute gas comparisons. Ultimately, comparisons were obtained using a 42 percent Argon and 58 percent Freon 13B1 mixture that showed the concept to be valid. Pressures, normalized to the static pressure at the nozzle exit, agree very well among the combustion products, and the Freon/Argon mixture, and M-O-C calculations in the two dimensional regions of the flow. There are some differences between the two sets of experiments in non-2D regions which we believe to be due to several factors, most of which are unique to the present experiments. The following sections describe in detail the results of the pressure measurements and our interpretation of their consequences. They are presented in chronological order because each set of data affected the design of the next step in our efforts to gain a complete understanding of the nozzle flow.

All the pressure data obtained are tabulated in Appendix B. Only centerline distributions of these data are plotted to indicate the trends and results of the experiments.

### Combustion Products

Our first crucial goal was to obtain accurate pressure measurements. The initial model design was such that the nozzle and tube assembly would move independently from the afterbody/cowl model, to eliminate the possibility of accelerations from the tube recoil reaching the pressure transducers. This turned out to cause more problems than it solved, because a rearward-facing step of about 0.8 mm in height resulted at the joint between the nozzle exit and model. This step produced an expansion and a reattachment shock wave that significantly influenced the pressures on the model. The steps did serve to illustrate the sensitivity of

the flow to small geometric changes, however. We also learned that the semiconductor strain gauge pressure transducers being used were extremely insensitive to acceleration, contrary to our previous experience with piezoelectric gauges. This allowed a model redesign to eliminate the steps by allowing direct contact from tube to model.

To illustrate the effect of the small step, Fig. 19 shows a comparison of the centerline pressure data obtained for the combustion gas with and without the step. Also shown is a two dimensional method of characteristics prediction of the no-step distribution with an approximation of the side wall expansion effect. All pressures have been normalized to the nozzle exit plane height,  $Y_3$ .

A centerline distribution on the cowl is shown in Fig. 20 along with a 2-D M-O-C calculation. Note that the measured pressures on both surfaces fall below the 2-D level sooner than the prediction. Figure 21 shows a planform view of the afterbody and indicates the region of measured 2-D level compared to the ideal region delineated by the expansion from the side walls. Ideally this expansion should be bounded by the Mach cone emanating from the corner where the nozzle and afterbody join. The Mach number governing the side wall expansion is that after the expansion of the flow onto the surface of the afterbody. The wide discrepancy between the expected and measured boundaries of the 2-D region apparently was partly due to the early arrival of three dimensional side wall influences, although lateral flow in the afterbody laminar boundary layer was also suspected as a partial cause, and many other possibilities were also investigated and found to be highly improbable.

To delay the side expansion influence we installed side plates (Fig. 9) that extended to the trailing edge of the cowl. The centerline afterbody distribution is shown with the side plates installed by the square symbols in Fig. 22. The triangles are the data obtained with no side plates. The 2-D calculation includes the delayed expansion from the side plates. Note that the pressure drop-off from the 2-D level was delayed, indicating that there is a significant effect from the side wall propagating through the boundary layer and arriving earlier than simple theory would predict. However, not all of the effect can be definitively attributed to this mechanism. With the side plates installed, the fall-off is even earlier relative to the new Mach line from the side wall afterbody juncture. Figure 23 is a planform view of the

## Afterbody C.L. Pressure Dist.

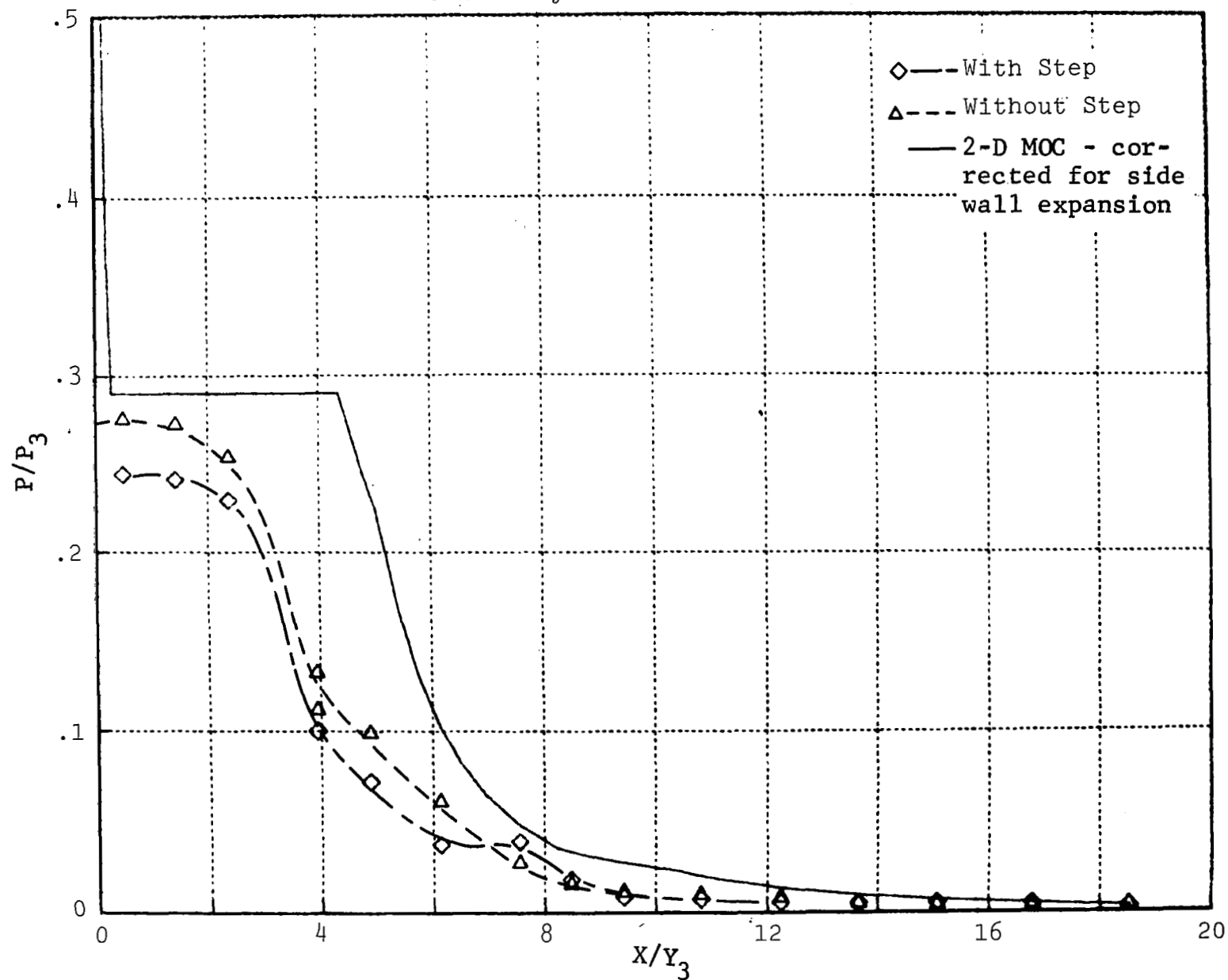


Fig. 19 Pressure Distribution on Afterbody Centerline - Comparison of Results with and Without Step at Nozzle Cowl Joint

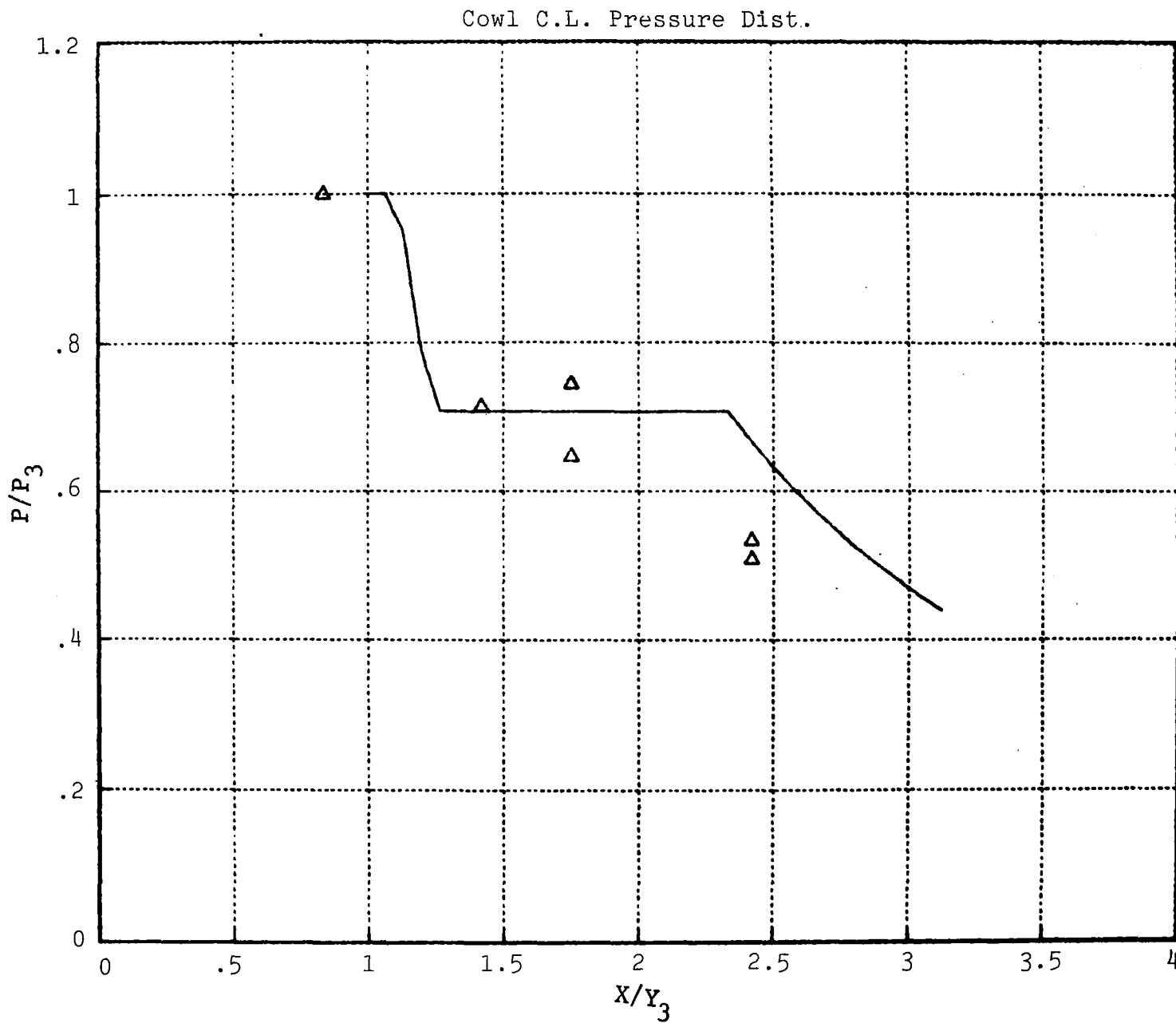


Fig. 20 Pressure Distribution on Cowl - Combustion Runs and Comparison with 2-D MOC Calculation

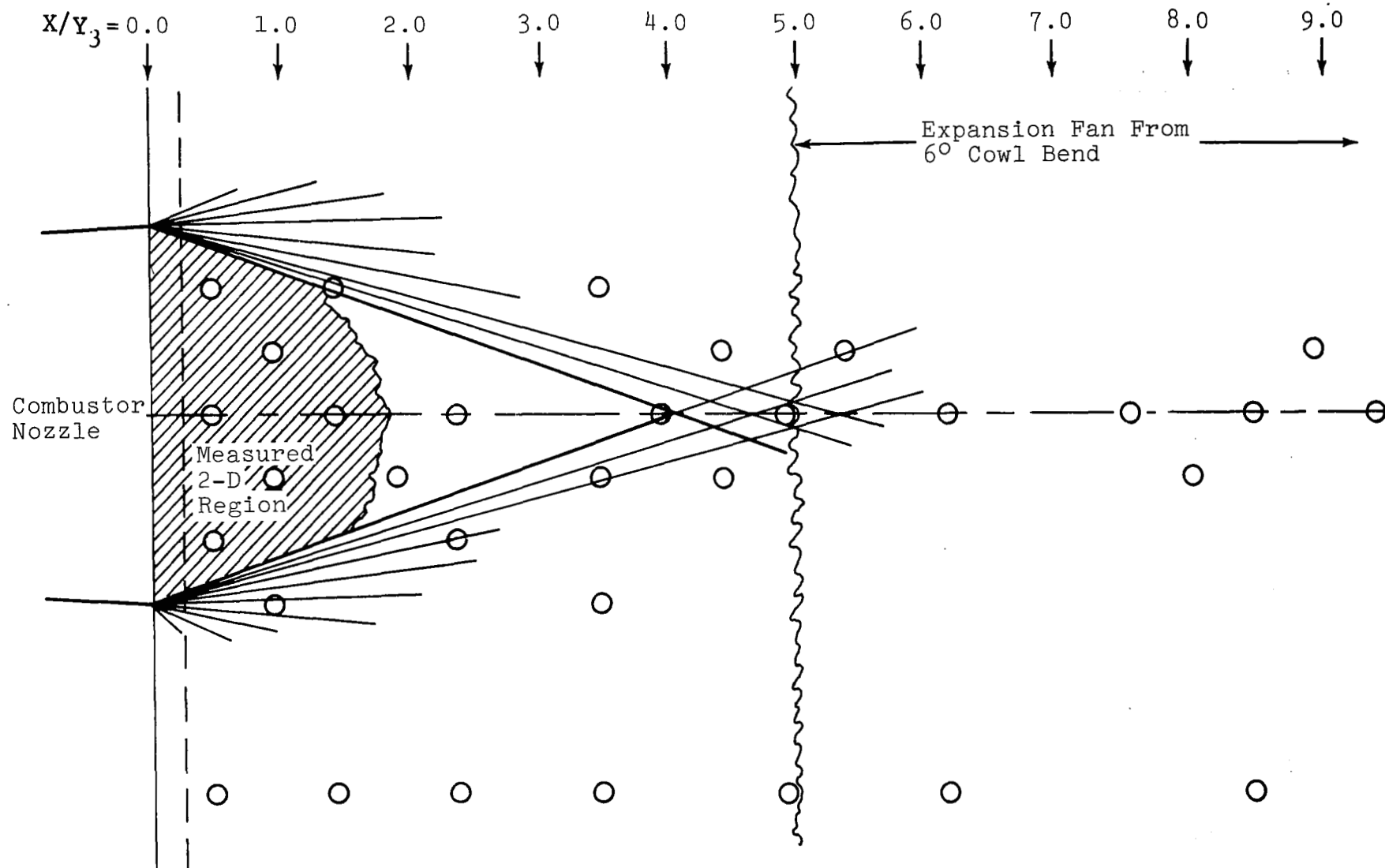


Fig. 21 Planform View of Afterbody Showing Ideal and Measured Two Dimensional Regions - No Side Plates

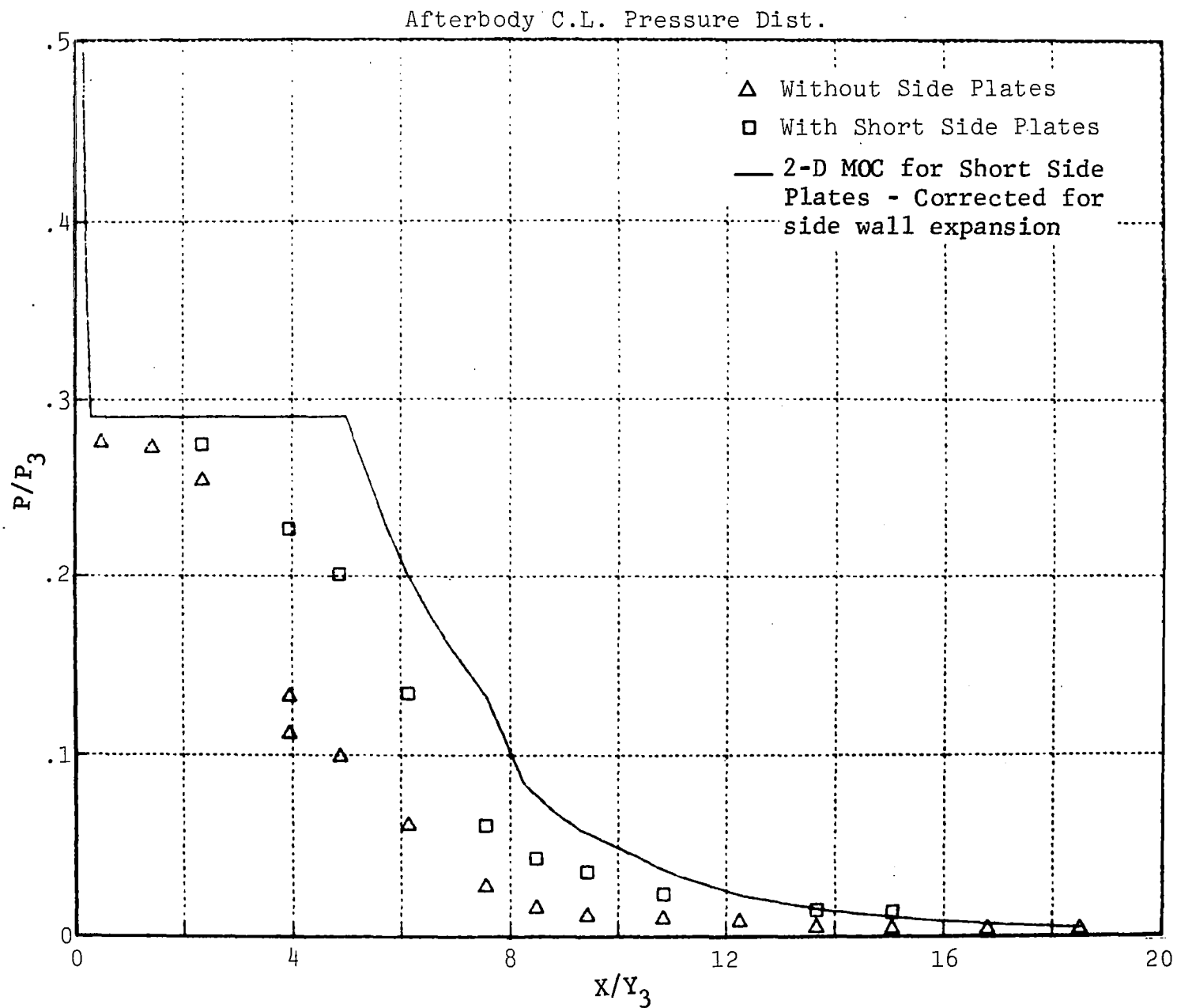


Fig. 22 Pressure Distribution on Afterbody Centerline With and Without Short Side Plates - Combustion Runs

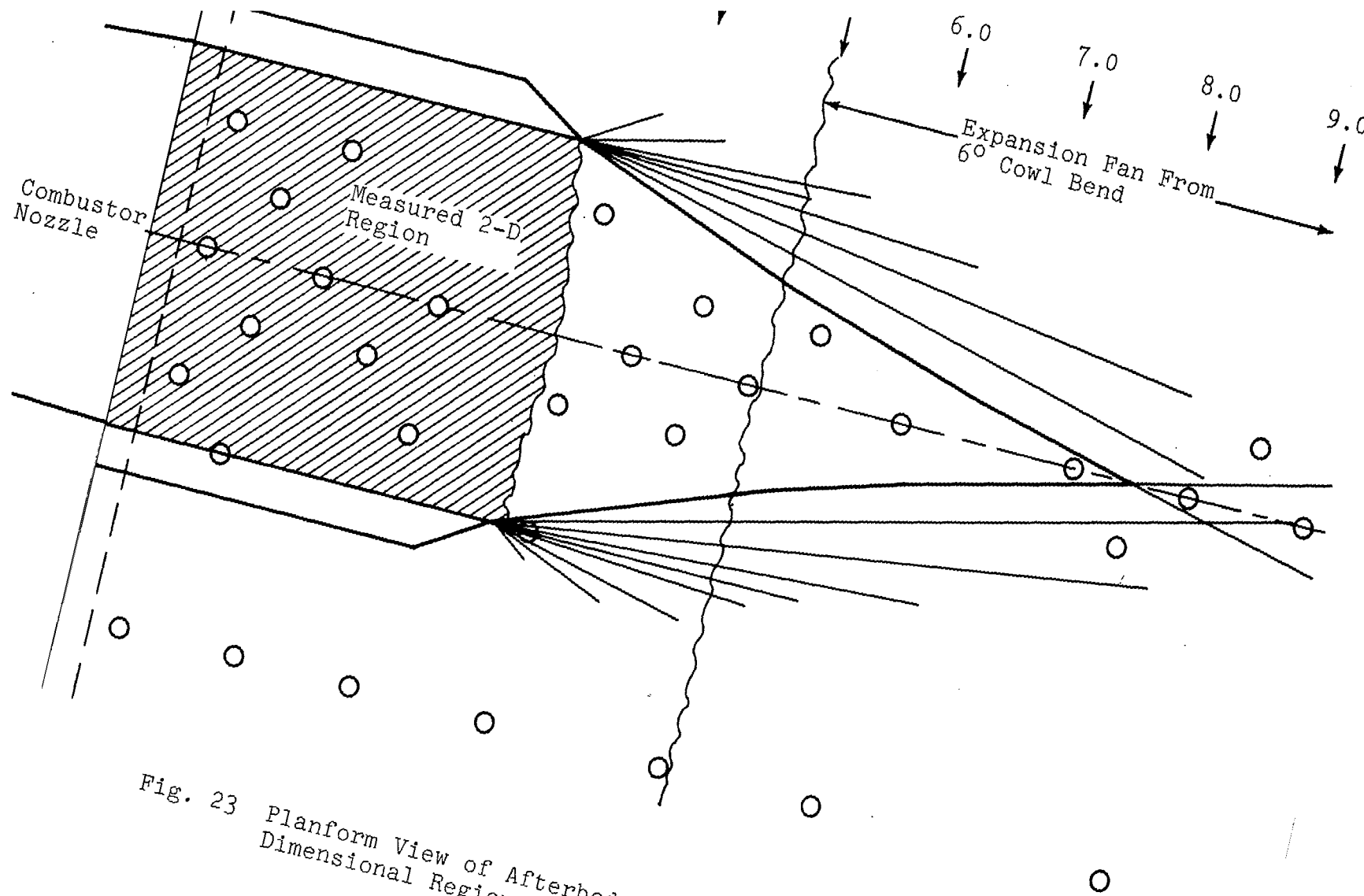


Fig. 23 Planform View of Afterbody Showing Measured and Ideal Two Dimensional Region - Short Side Plates

afterbody and end plates. The measured 2-D region is indicated. Beyond an  $X/Y_3$  of about 5, the 6 degree expansion on the cowl is felt on the afterbody, so the rapid fall-off in pressure in this region is expected. However, between the end of the end plates ( $X/Y_3 \approx 3.2$ ) and the region of influence from the cowl expansion, the pressure distribution appears to have been influenced by an additional expansion and recompression. A close inspection of the model revealed a very slight mismatch still existing at the joint of the nozzle and cowl. Figure 17 shows the estimated extent of this mismatch. The influence of this geometrical approximation on the afterbody pressure distribution was calculated as discussed previously and the result is shown in Fig. 24 along with the data obtained in the ideal 2-D region. The solid points are those obtained off the centerline but within the theoretical 2-D region. This appears to explain the distributions we are seeing. As a check, side plates extending to an  $X/Y_3$  of about 9 were installed and the tests repeated. A similar phenomenon was observed (Fig. 24), though the levels were slightly different. The significantly higher pressure levels beyond  $X/Y_3$  of 7 in Fig. 24 are due to the fact that the longer end plates prevent any side wall expansion effects from reaching the centerline in the measurement region. The wide scatter of points where the reattachment shock is postulated to hit the afterbody ( $X/Y_3 \approx 3.5$ ) is consistent with the steep gradients that would exist in such a flow.

### Substitute Gas Comparison

A mixture of 42 percent Argon and 58 percent Freon 13B1 was chosen as the substitute gas for this investigation. The running conditions for this gas are described earlier in this report. This mixture was chosen because it required the lowest stagnation temperature of those mixtures investigated in Ref. 1 (an advantage for wind tunnel testing). No attempt has been made to alter the mixture to improve the results. All substitute gas comparisons were run with the short end plates installed on the model.

The nozzle used to achieve the desired exit plane conditions in the test section was originally designed for the combustion products. While the thermodynamic behavior of the substitute gas blend is excellently matched to that of the combustion gases for those portions of their respective flows that cover the cowl and afterbody, the quality of the match degrades for the flow upstream



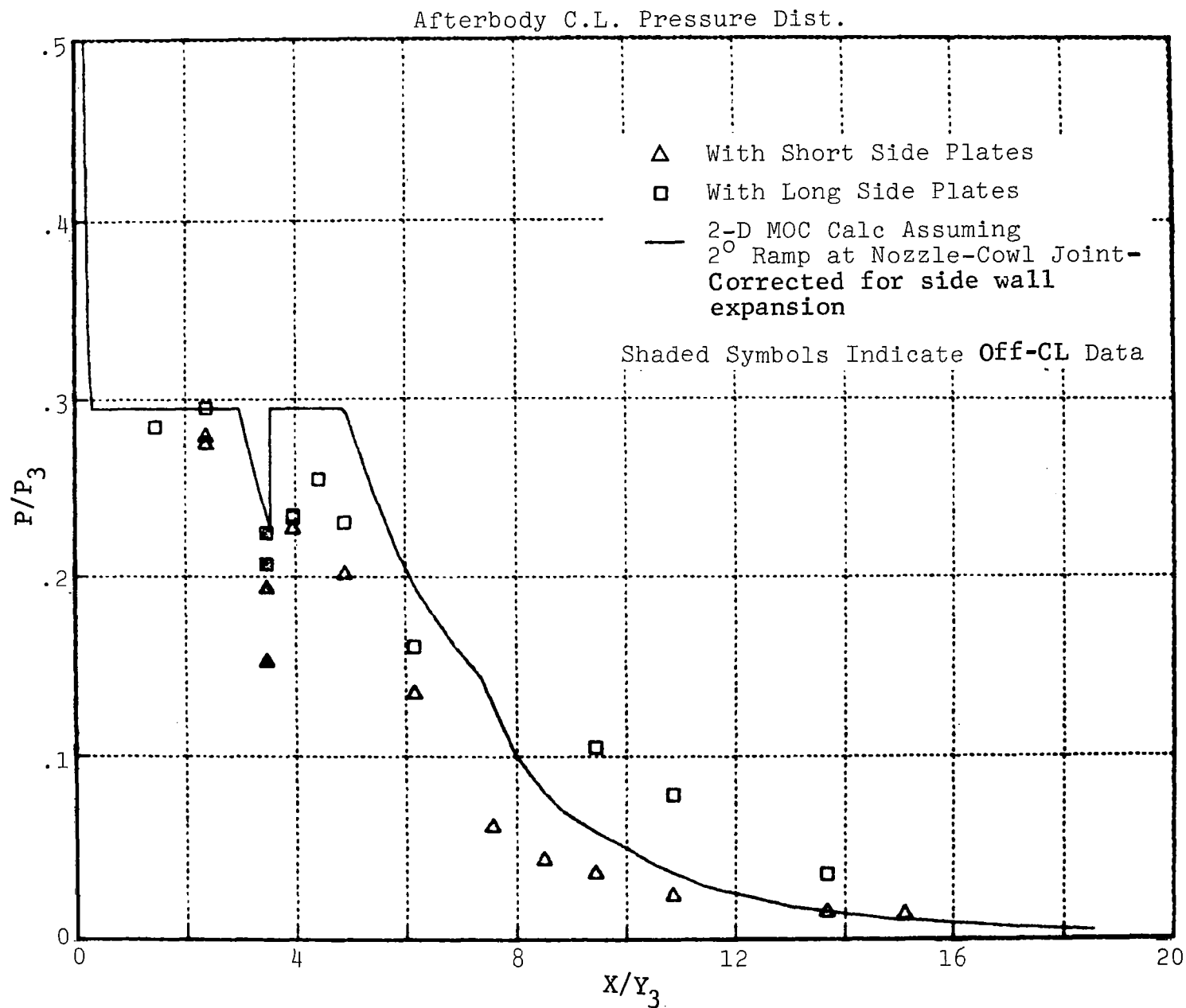


Fig. 24 Pressure Distribution on Afterbody-Combustion Runs - Short and Long Side Plates - Comparison with 2-D M-O-C Calculation Assuming  $2^\circ$  Ramp at Nozzle-Cowl Joint

of the combustor exit plane. The nozzle that establishes exit plane conditions should therefore have slightly different contours for the substitute gas than for the combustion gas. Calculations showed that the substitute gas run through the combustion nozzle would give a reasonable match at the exit plane, but the effect of the resulting slight nonuniformities within the nozzle on the pressure distributions was unknown. These effects appear to be more significant than we expected.

Figure 25 shows the pressures in the cowl 2-D region for both the substitute gas and combustion products. The agreement is good, implying that the flow departs from 2-D the same way in both gases.

Figure 26 shows the comparison of pressure distributions between the two gases on the centerline of the afterbody. First, note that the agreement in the region where a 2-D distribution prevails is excellent. Both gases expand to a relative pressure of about 28 percent of the nozzle exit pressure. The substitute gas is therefore behaving in a manner very similar to that of the combustion gas, as it should. There appears to be a local compression in the flow of the substitute gas near the downstream boundary of the 2-D region that does not appear for the combustion products. This compression shows up repeatedly as a higher pressure for the substitute gas at an  $X/Y_3$  of 5 on the centerline. Off-centerline, and in the region of 3-D flow, the substitute gas pressures measured at a  $X/Y_3$  of 3.4 (not shown) are double those for the combustion gas and higher even than the calculated 2-D value. Beyond  $X/Y_3$  of 5 the substitute gas appears to parallel the combustion gas expansion, at a slightly higher level due to the compression earlier in the flow.

The reasons for the strong compression wave appearing in the substitute gas flow and not in the combustion gas appear to be associated with flow nonuniformities originating inside the nozzle. We know the nozzle design to be slightly mismatched to the substitute gas, and the flow to be very susceptible to slight nonuniformities. Waves generated internally could be propagating from the nozzle and affecting the pressures. Because the boundary layer on the afterbody is laminar (see Heat Transfer subsection), the disturbances would be spread over a wider region on the plate compared to those for a turbulent boundary layer.

Further evidence that a mismatched nozzle could be the cause of the differences was obtained when the substitute gas was run through a nozzle with a throat size that gave an exit Mach number

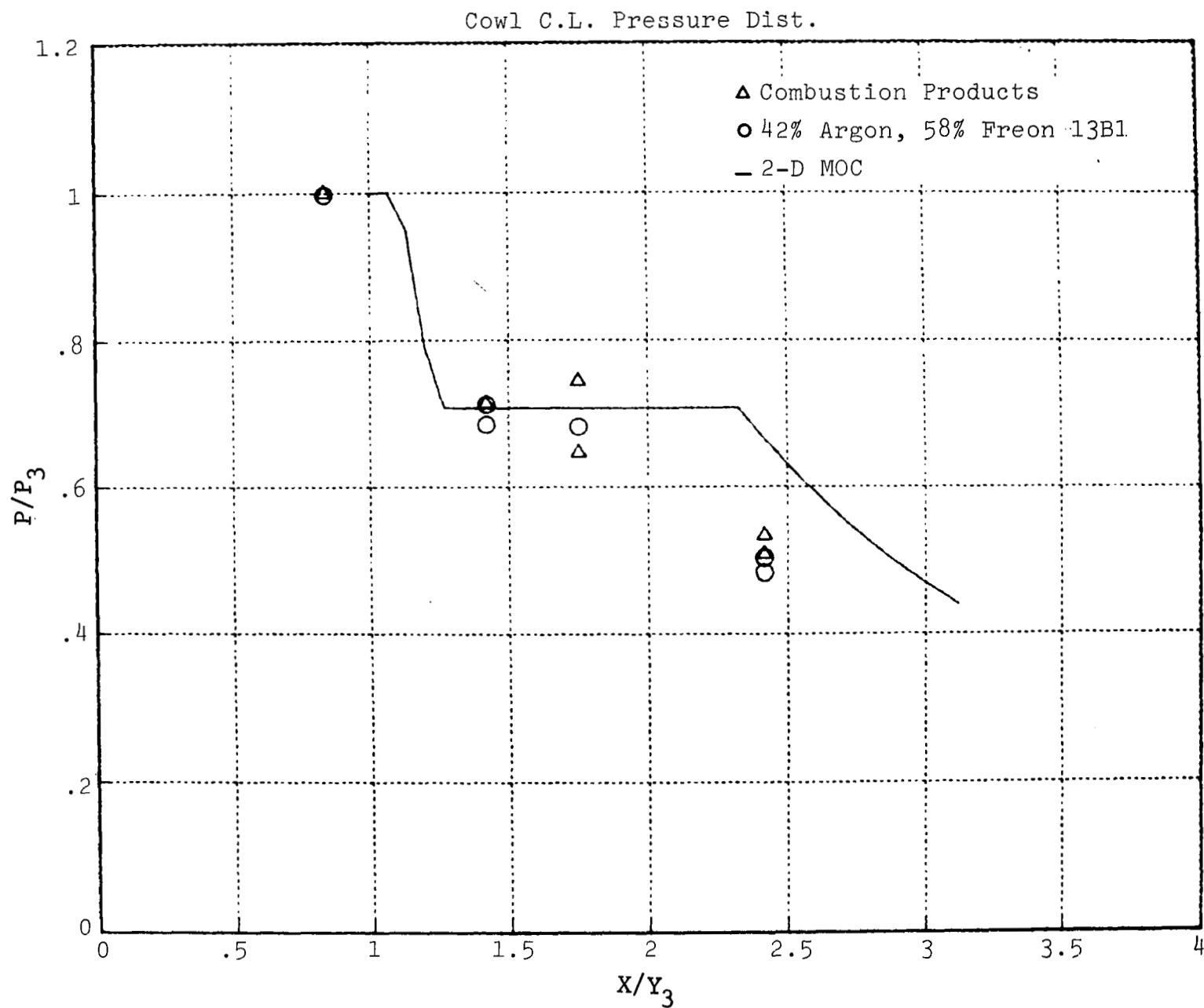


Fig. 25 Cowl Pressure Distribution - Comparison of Combustion With Substitute Gas Results

# Afterbody C.L. Pressure Dist.

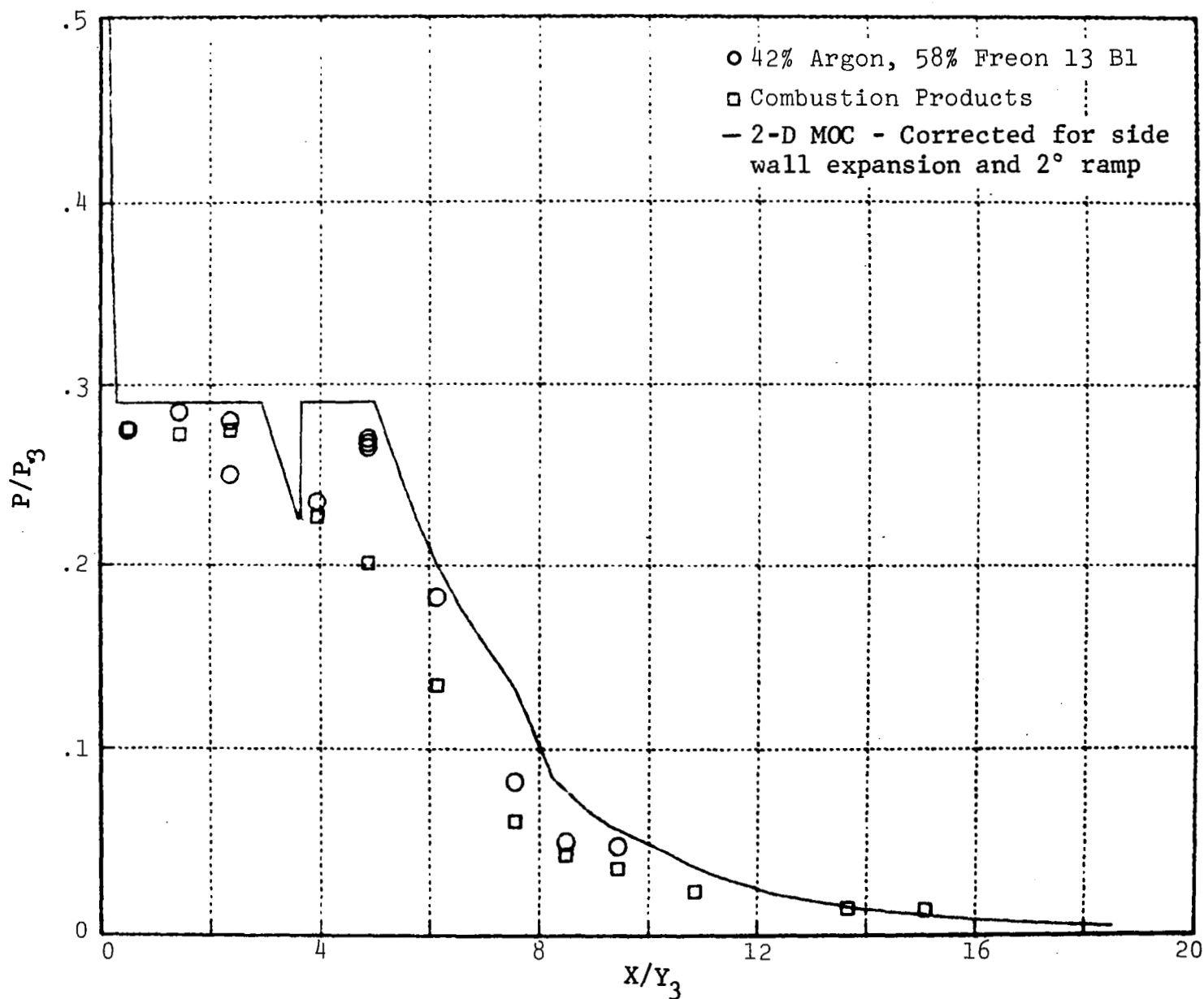


Fig. 26 Afterbody Centerline Pressure Distributions - Comparison of Combustion with Substitute Gas Results - Short Side Plates

of about 2.55 rather than the design value of 2.35. Figure 27 shows the data obtained on the afterbody centerline. The off-design nozzle produced obvious waves that resulted in a very non-uniform pressure distribution on the afterbody.

One final point should be made concerning the substitute gas results. The pressure levels that we measured were approximately 25 times lower for the substitute gas than for the combustion gas. This meant running the shock tube at a stagnation pressure of  $4.14 \times 10^5 \text{ N/m}^2$  for the substitute gas. This is very low for a shock tunnel, and led to difficulties in obtaining a good quality shock system in the driven tube. Nonidealities might have resulted, causing the state of the substitute gas to be somewhat different from that calculated.

### Heat Transfer

Heat transfer rates due to the flow of combustion products were measured on the afterbody and cowl. The results are tabulated in Table 5. The centerline distribution on the afterbody is shown in Fig. 28. Assuming a reasonable virtual origin the fall-off with distance is close to the  $X^{-\frac{1}{2}}$  character of a zero pressure gradient laminar boundary layer. In addition we have been informed that the heat transfer rates agree with laminar calculations performed by Talcott and Hunt of Langley Research Center using the "BLIMP" program reported in Air Force Weapons Lab Report FWL TR-69-114. Turbulent heating rates were calculated using the method in Ref. 9, and the results gave rates an order of magnitude higher than the measured values.

The fact that the afterbody boundary layer is laminar is not an artifact of the facility or the simulation technique. All runs were made at the full scale flight Reynolds number. The laminar boundary layer will be much more responsive to inviscid flow disturbances than would a turbulent one, and could be a contributing factor to the anomalies in the pressure data.

### Infrared Radiation from Nozzle Exit Plane

The spectral radiance at the exit plane of the nozzle was measured between 2.4 and 4.8 microns, using a rapid scan circular variable filter (CVF) spectrometer (designed by the Chemical Physics Branch of the Grumman Research Department). Essential components of the spectrometer are: 1) a liquid nitrogen

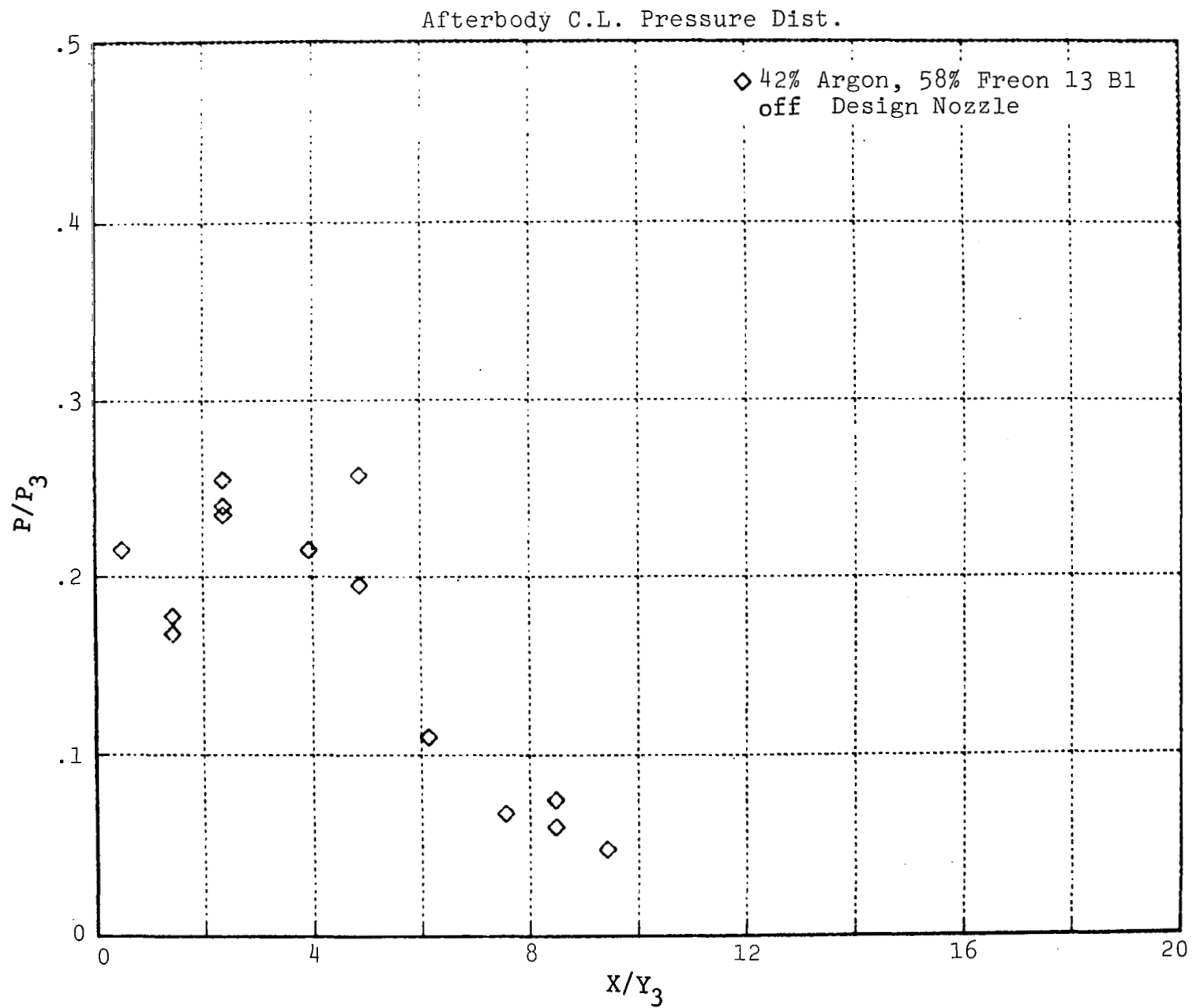


Fig. 27 Afterbody Centerline Pressure Distribution for Substitute Gas Run Through Off-Design Nozzle

TABLE 5 HEAT TRANSFER DATA

Nondimensional Axial Distance from Exit Plane $X/Y_3$	Nondimensional Transverse Distance from Centerline $Z/Y_3$	$\dot{q}$ gm cal/ cm <sup>2</sup> . sec
Cowl		
0.333	0	37.94
0.333	0.5	36.86
0.333	1.667	10.33
1.75	0.833	19.32
1.75	1.167	17.29
3	0.5	10.92
Afterbody		
0.955	0	19.16
1.897	0	14.36
3.465	0	8.64
6.837	0	4.17
10.131	0	1.83
12.954	0	0.835
1.426	0.5	13.28
2.367	0.5	12.71
2.367	1	11.27
2.367	1.5	6.26

cooled InSb detector, 2) a CVF rotating at 16,000 rpm with a resolution at 3 microns of 0.03 micron, and 3) an Irtran 2 optical system. Calibration was performed against a blackbody source (NBS traceable temperature).

A typical IR spectral radiance measurement is shown in Fig. 29 where a comparison is made with a theoretical prediction using an IR band model code (Ref. 10). The measured spectrum clearly exhibits the 2.7 micron water band, extending almost to 4 microns, and the lower wavelength wing of the 6.3 micron fundamental of water, between 4 and 4.8 microns. The measured and predicted spectra are in good agreement, especially when one considers the experimental uncertainty and imperfections of

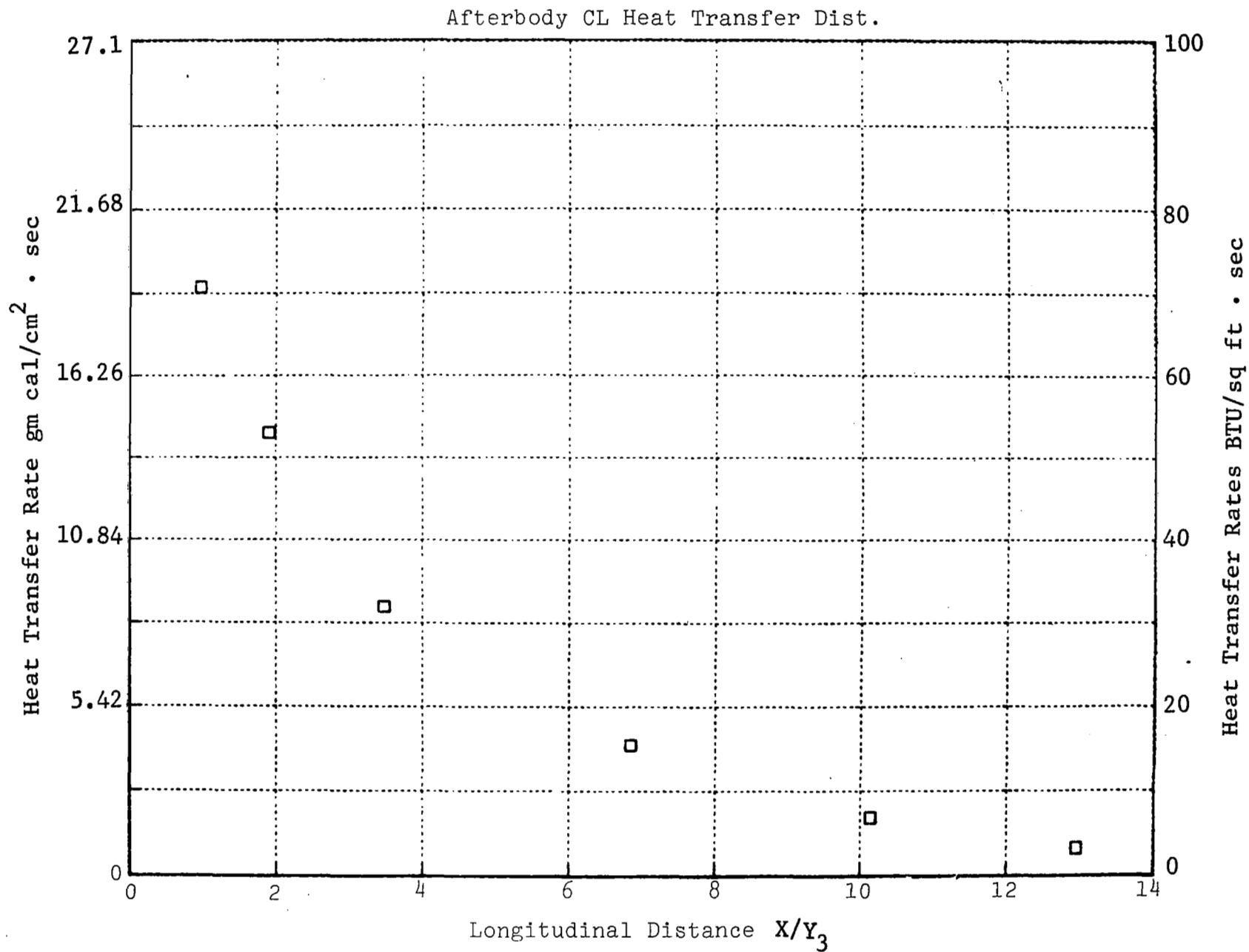


Fig. 28 Heat Transfer Distribution Along Afterbody Centerline



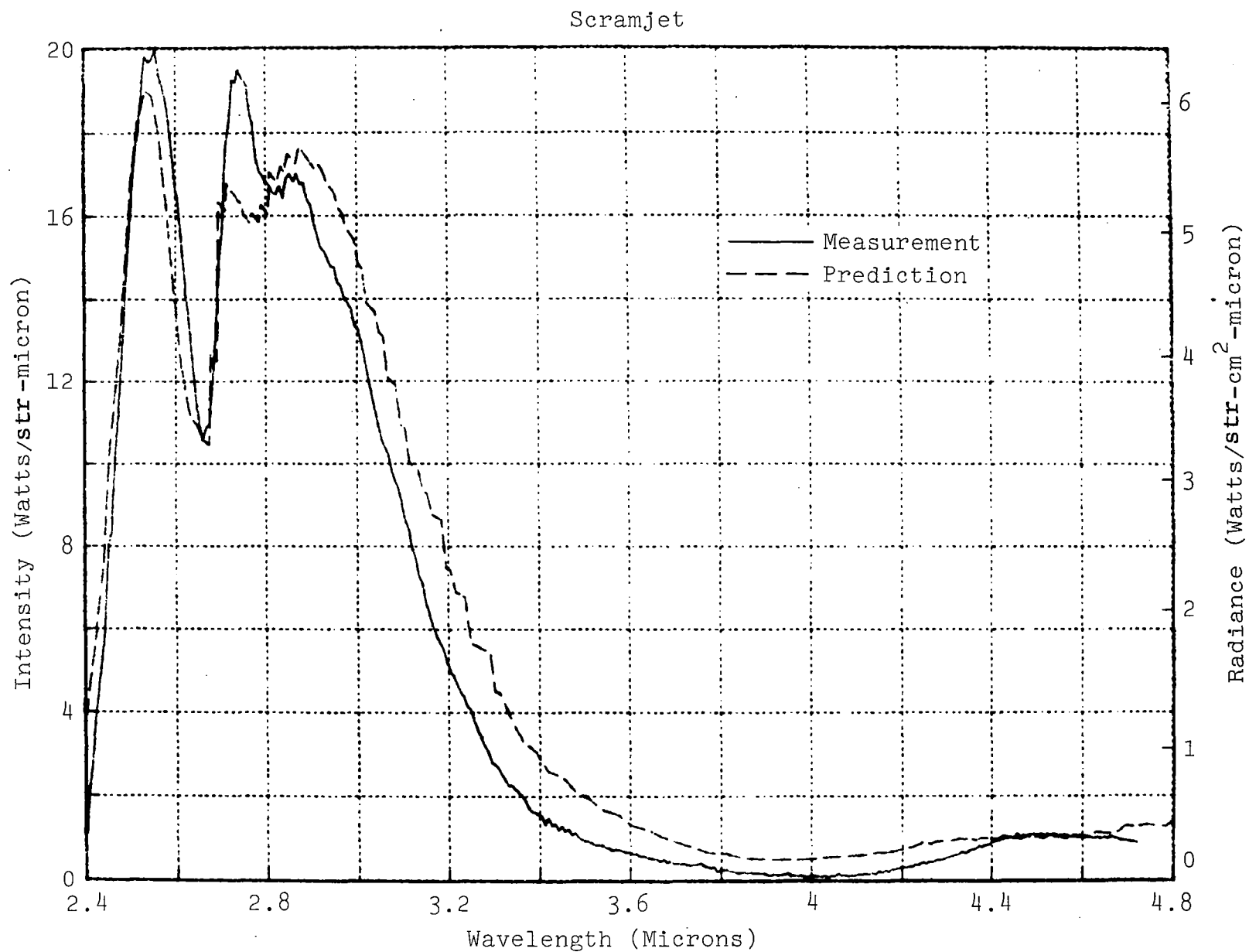


Fig. 29 Comparison of Calculated and Measured Infrared Emission From Nozzle Exit Plane

theoretical band model codes (high temperature absorption coefficients  $\pm 10$  percent). From Fig. 29 we conclude that the experimental temperature and species concentration are sufficiently accurate to give excellent simulation. Note that the radiance at 2.7 microns is proportional to a power greater than 3 of the temperature, so that the differences between experiment and theory in Fig. 29 should be attributed to about a 4 percent difference between the theoretical and experimental temperature. The agreement with theory in Fig. 29 is also typical of previous measurements which attest to the excellent simulation which can be achieved with the detonation tube facility in a wide variety of combustion systems.

### Impact Pressure Measurements

To further verify the gas state in the vicinity of the exit plane of the combustor nozzle, a series of runs were made with both combustion and substitute gas to measure the impact pressure at the stagnation point of a flat-faced probe. Kistler Model 603 pressure transducers were mounted in 0.792 cm diameter (0.312 in.) flat-faced probes and located at various axial positions from 4.763 cm (1.875 in.) within the nozzle to the nozzle exit plane. Measurements were also made at off-axial locations ranging from  $\pm 0.953$  cm (0.375 in.) in the Y-direction to  $\pm 5.08$  cm (2.0 in.) in the Z-direction. Typical impact pressure oscilloscope records for both combustion and substitute gas are shown in Fig. 30. The measurements indicated a steady uniform core flow within the region covered.

The substitute gas impact pressure measurements agreed reasonably well with ideal gas theory, considering the uncertainties in the state of the substitute gas discussed previously. Curves of ideal gas  $P_{T1}/P_{T2}$  ratio (Ref. 11) for various values of  $\gamma$  and free stream Mach number are shown in Fig. 31. In the uniform flow region of our nozzle, the measured  $P_{T1}/P_{T2}$  ratio was  $2.06 \pm 0.06$ . Based on our measured static pressure ratio, our free stream Mach number was 2.4. The measured total pressure ratio is plotted in Fig. 31. It falls on the line of  $\gamma = 1.25$  for  $M = 2.4$ , which is a little higher  $\gamma$  than we expected, but the use of the total pressure ratio to determine the value of  $\gamma$  could lead to error. For instance, any vibrational freezing of the

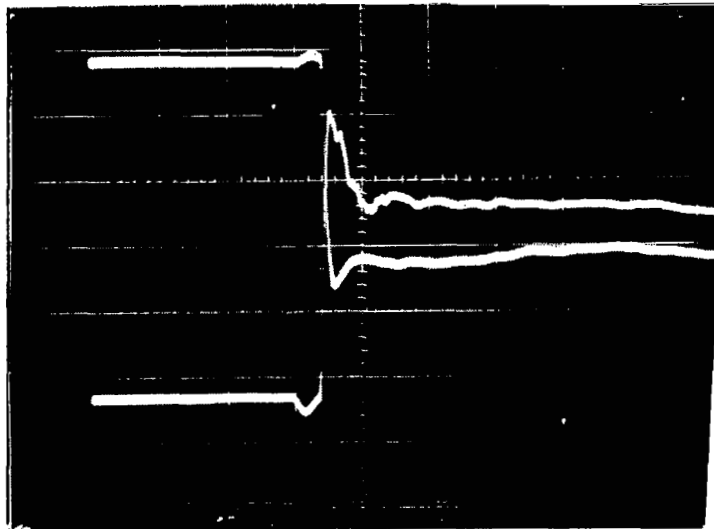


Fig. 30a Oscilloscope Record of Combustion Gas Impact Pressure at Nozzle Exit Plane. Horizontal Sweep: 0.5 msec/cm, Left to Right. Vertical Deflection Both Beams:  $1.38 \times 10^6$  N/m<sup>2</sup>/cm.

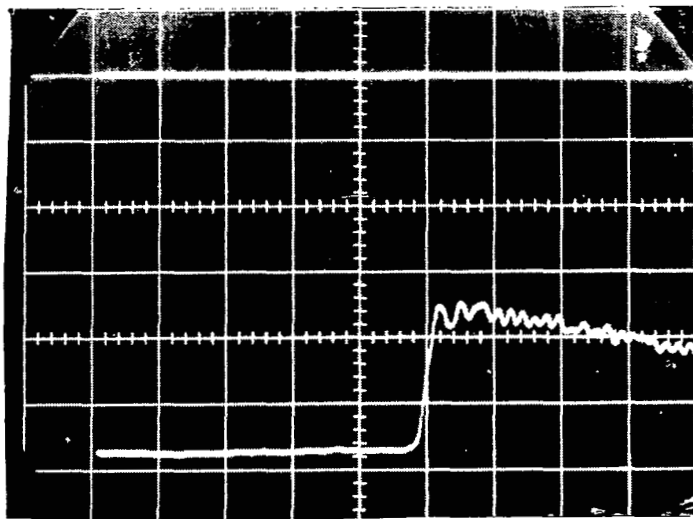


Fig. 30b Oscilloscope Record of Substitute Gas Impact Pressure at Nozzle Exit Plane. Horizontal Sweep: 1.0 msec/cm, Left to Right. Vertical Deflection:  $1.03 \times 10^5$  N/m<sup>2</sup>/cm.

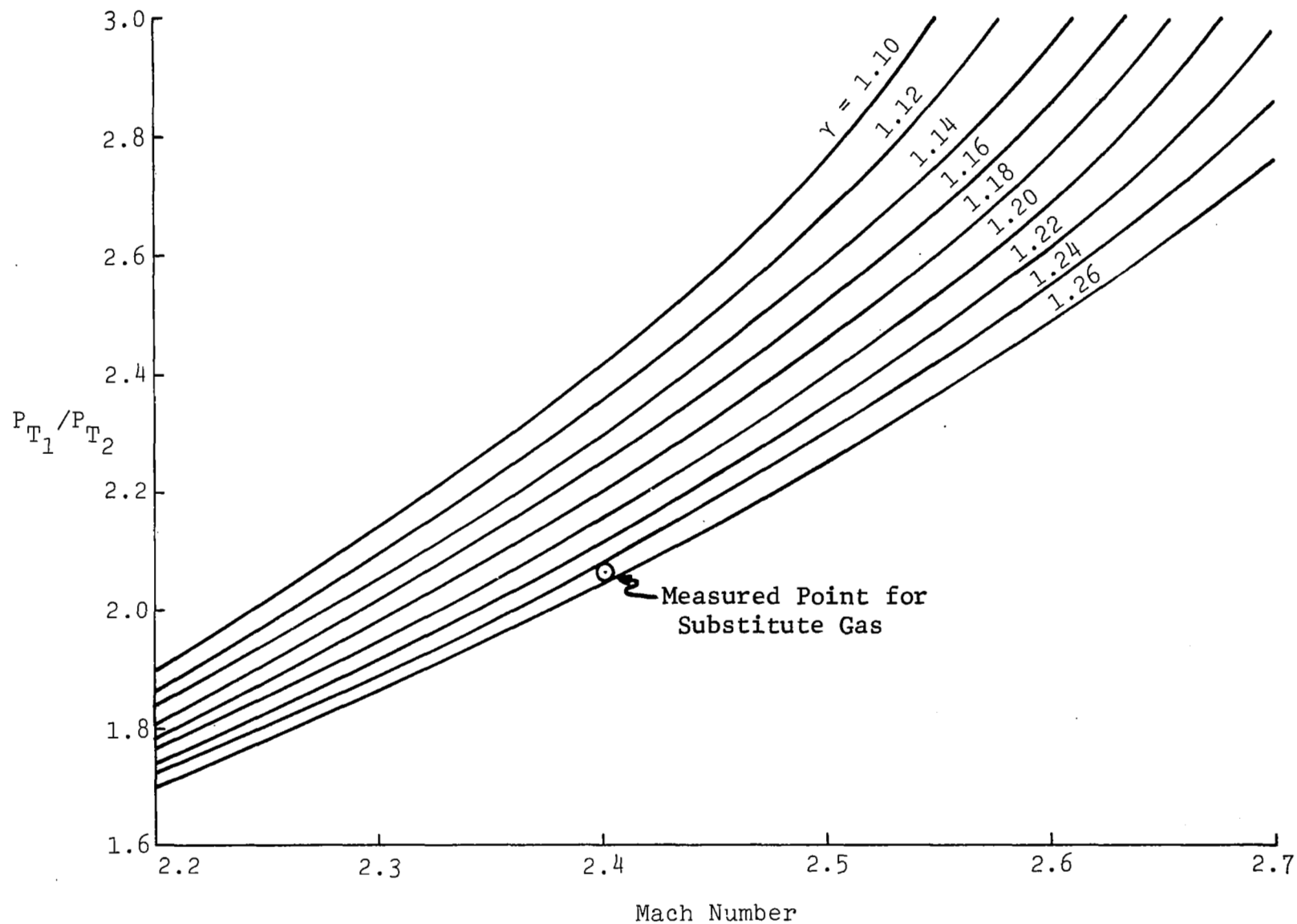


Fig. 31 Ratio of  $P_{T1}/P_{T2}$  vs Mach Number for Different Values of  $\gamma$  (Ideal Gas)

complex Freon molecule between the probe's bow shock and its face could tend to increase the effective  $\gamma$  of the gas.

The combustion gas impact pressure measurements all read approximately 15 percent too low. We expected pressures on the order of  $4.8 \times 10^6 \text{ N/m}^2$  (700 psia) to  $5.2 \times 10^6 \text{ N/m}^2$  (750 psia), depending on the nature of the probe stagnation process. The measurements were always  $4.14 \times 10^6 \text{ N/m}^2$  (600 psia). The pressure signals looked quite good (see Fig. 30). The transducer diaphragms were thermally protected with a thin layer of an RTV compound, and the signals showed none of the characteristic decay associated with temperature effects. The signals were filtered to eliminate high frequency ringing, which is always present with this type of impact pressure transducer, but there was no low frequency oscillation superimposed on the mean level, which might be indicative of probe acceleration. We made a run with a transducer sealed off from the flow to check for acceleration effects, but that transducer showed no signal. The identical probe and transducer was used for both the substitute gas and combustion runs. All circuits were carefully checked and the runs repeated several times so we have absolutely no indication that the measurement is incorrect.

For data analysis, we assumed six different types of probe and nozzle flow fields and calculated the expected impact pressures. Most of the calculations were done in two steps with the computer program of Ref. 4. The first step was to determine the free stream static properties, velocity, and composition at a state corresponding to the measured value of  $P_3$ . The second step was to determine the static properties behind a normal shock whose incident conditions were the pressure, temperature, velocity, and composition as determined by the first step. We then used the ideal gas equation

$$\frac{P_o}{P} = \left( 1 + \frac{\gamma - 1}{2} M^2 \right)^{\gamma/(\gamma-1)}$$

to calculate the isentropic compression from behind the shock to the stagnation point on the probe face. Use of this equation is justified on the grounds that 90 percent of the recompression takes place across the shock wave where real gas effects are taken into account by the calculations. In the last 10 percent of the recompression, the change in  $\gamma$  is very small. In all the calculations we assumed the nozzle stagnation pressure to be the measured value of  $P_5$ ,  $1.068 \times 10^7 \text{ N/m}^2$ , the nozzle stagnation

enthalpy to be 578.4 cal/gm, and the nozzle exit plane static pressure to be the measured value of  $7.031 \times 10^5 \text{ N/m}^2$ . In the first flow field we assumed complete equilibrium flow through the nozzle and across the bow shock to the stagnation point on the probe. This gave us an impact pressure of  $4.944 \times 10^6 \text{ N/m}^2$  (717.3 psia). In the second flow field we assumed full equilibrium through the nozzle expansion, but frozen composition across the probe bow shock. This produced an impact pressure of  $4.876 \times 10^6 \text{ N/m}^2$  (707.4 psia). In the third calculation we assumed the nozzle flow composition frozen at the throat, but returned to equilibrium behind the probe bow shock. This produced an impact pressure of  $5.177 \times 10^6 \text{ N/m}^2$  (751.0 psia). The fourth calculation assumed the nozzle flow composition frozen at the throat and remained frozen across the bow shock. This produced an impact pressure of  $5.148 \times 10^6 \text{ N/m}^2$  (746.9 psia). In the fifth and sixth calculations we assumed a one dimensional, finite rate chemistry flow field, starting the finite rate calculation in the subsonic region before the throat. The computer program of Ref. 12 was used for this calculation, with the best  $\text{H}_2/\text{Air}$  rate constants currently available. In these calculations we assumed a one dimensional area distribution that gave us approximately the nozzle centerline pressure distribution calculated by the M-O-C program. In the fifth case we assumed the flow returned to equilibrium behind the probe bow shock. This produced an impact pressure of  $4.971 \times 10^6 \text{ N/m}^2$  (721.1 psia). The sixth calculation assumed the composition was frozen across the bow shock. This produced an impact pressure of  $4.911 \times 10^6 \text{ N/m}^2$  (712.4 psia). In none of these calculations could we arrive at an impact pressure near the measured value of  $4.14 \times 10^6 \text{ N/m}^2$ .

We also investigated the possibility that internal degrees of freedom could be frozen in the nozzle expansion. By comparison to detailed calculations previously done for rocket exhaust radiation prediction (which were very precisely confirmed by experiment), we were able to verify that vibrational lag in  $\text{N}_2$  would be negligible in the present expansion. Our case has higher pressures, a much longer flow path, and only a slightly higher velocity than cases for which vibrational lag was negligible from the former work. The  $\text{N}_2$  system has by far the slowest vibrational decay rate of any of the molecules in the flow.

If we plot the measured value of  $P_{T1}/P_{T2}$  on the ideal curves of Fig. 31 we can see the extent of the anomaly. The measured value of the impact pressure should be higher, or the flow Mach number must be 0.1 to 0.2 greater than we think it is,

and this would be very inconsistent with the measured value of  $P_5/P_3$ . Further investigation of this problem is clearly indicated.

## 6. CONCLUSIONS AND RECOMMENDATIONS

The detonation tube provides a good simulation of the exhaust flow from a hydrogen/oxygen scramjet engine. Pressure distributions obtained on a cowl model and afterbody with the simulated flow of combustion products and flow from a substitute gas mixture of 42 percent Argon and 58 percent Freon 13B1, were in agreement in the two dimensional regions of the flow. Except for a few explainable variations, pressure distributions also followed the three dimensional behavior. The flows of both the combustion products and substitute gas were highly sensitive to very small perturbations in the nozzle and model geometries, and nonidealities in nozzle design.

Only one substitute gas choice has been tested thoroughly on the scramjet model. Although no unexpected behavior can presently be attributed to the substitute gas, it will probably be desirable to investigate variations in the blend in future refinements of the technique. Departures in the substitute gas pressures from those of the combustion products all appear to be explained by nozzle mismatches outside the range in which the gases are expected to behave the same. It will also be necessary to investigate other flow problems, such as segmented nozzles, shocks in the flow, and different flight conditions. These types of investigations are recommended for future work. Further investigation of anomalously low impact pressures in the combustion gas flow is also warranted.

In any future experiments the nozzle contours must be designed specifically for the gas to be used, taking into account property variations upstream of the matching region. We learned that it is not sufficient to match only the exit plane properties. With proper attention to model and nozzle fidelity, we are confident that future experiments will give a highly accurate simulation for the X-24C flight vehicle.



## 7. REFERENCES

1. Oman, R., Foreman, K., Leng, J., and Hopkins, H., "Simulation of Hypersonic Scramjet Exhaust," NASA CR-2494, March 1975.
2. Hopkins, H., Konopka, W., Leng, J., and Oman, R., "Simulation Experiments Using Hydrogen/Oxygen Gas Mixtures in a High-Pressure Detonation Tube," Final Report, Contract No. NAS 9-12447, Grumman Research Department Report RE-456, May 1973; also published as NASA Report MSC-05836.
3. Leng, J., Oman, R., and Hopkins, H., "A Detonation Tube Technique for Simulating Rocket Plumes in a Space Environment," J. Spacecraft and Rockets, Vol. 5, No. 10, pp. 1148-1154, October 1968.
4. Svehla, R. and McBride, B., "FORTRAN IV Computer Program for Calculation of Thermodynamic and Transport Properties of Complex Chemical Systems," NASA TN-D-7056, January 1973.
5. Ratcliff, A. W., Smith, S. D., and Penny, M. M., "Rocket Exhaust Plume Computer Program Improvement, Vol. I - Final Report, Summary Volume, Method-of-Characteristics Nozzle and Plume Programs," Lockheed Missiles and Space Company, LMSC/HREC D162220-I, NASA STAR N72-18942, January 1972.
6. Crown, J. C., "Design of Nozzles Having Continuous Wall Curvature," Journal of the Aeronautical Sciences, Vol. 19, No. 5, pp. 358-359, May 1952.
7. Konopka, W., "Heat Transfer Instrumentation for the Grumman Hypersonic Shock Tunnel," Grumman Research Department Memorandum RM-387, July 1965.
8. Dyner, H. B., "Density Variation Due to Reflected Shock-Boundary-Layer Interaction," The Physics of Fluids, Vol. 9, No. 5, pp. 879-892, May 1966.
9. Weingold, H. and Zupnik, T., "The ICRPG Turbulent Boundary Layer Reference Program," Pratt and Whitney Aircraft, July 1969, AD 841202; NASA X69-14708.

10. Martinsen, R. and Fishbein, E., "A Fine Spectral Resolution (FSR) Program for the Calculation of Infrared Radiation Emitted by Exhaust Plumes," Grumman Research Department Memorandum RM-575, July 1973.
11. Liepmann, H. W. and Roshko, A., Elements of Gasdynamics, John Wiley & Sons, Inc., New York, 1957.
12. Kliegel, J. R., Nickerson, G. R., Frey, H. M., Quan, V., and Melde, J. E., "ICRPG Two Dimensional Kinetic Nozzle Analysis Computer Program," Dynamic Science, July 1968. AD 871338. Improved Version, December 1970.

# APPENDIX A

## ON THE CALCULATION OF THE PROPERTIES OF SUBSTITUTE GAS MIXTURES

The specific heat for a mixture of perfect gases is

$$C_p = \sum X_i C_{p_i}$$

where  $X_i$  is the mole fraction of each component.

The freons with which we are dealing are calorically imperfect and  $C_p$  is a function of temperature

$$\therefore C_p(T) = \sum X_i C_{p_i}(T)$$

To compute the Mach number as a function of  $C_p(T)$  we write the steady flow energy equation as

$$h_1 + \frac{1}{2} U_1^2 = h_2 + \frac{1}{2} U_2^2 \equiv H_0$$

The enthalpies,  $h$  and  $H$ , are the integral of  $C_p(T)dT$  from  $T = 0$  to  $T = T_2, 1$ , or  $0$ .

The energy equation becomes

$$\int_0^{T_1} C_p(T) dT + \frac{1}{2} U_1^2 = \int_0^{T_2} C_p(T) dT + \frac{1}{2} U_2^2 = \int_0^{T_0} C_p(T) dT$$

The velocity at state (1) is then

$$\frac{1}{2} U_1^2 = \int_0^{T_0} C_p(T) dT - \int_0^{T_1} C_p(T) dT = \int_{T_1}^{T_0} C_p(T) dT$$

and the Mach number

$$M_1 \equiv \frac{U_1}{a_1} = \sqrt{\frac{2 \int_{T_1}^{T_o} C_p(T) dT}{\gamma_1 R T_1}}$$

To evaluate the integral we fit a fourth order polynomial through the  $C_p(T)$  versus  $T$  data, over the range of interest

$$C_p(T) = AT^4 + BT^3 + CT^2 + DT + E$$

$$\begin{aligned} \therefore \int_{T_1}^{T_o} C_p(T) dT &= \frac{A}{5} (T_o^5 - T_1^5) + \frac{B}{4} (T_o^4 - T_1^4) + \frac{C}{3} (T_o^3 - T_1^3) \\ &\quad + \frac{D}{2} (T_o^2 - T_1^2) + E(T_o - T_1) \end{aligned}$$

$\gamma_1$  is computed from the value of  $C_p(T)$  at  $T_1$

$$\gamma_1 = \frac{C_p(T_1)}{C_p(T_1) - R}$$

Thus, for any assumed stagnation temperature,  $T_o$ , a Mach number versus  $T$  table can be computed.  $\gamma$  and  $C_p$  are known functions of  $T$ , independent of the choice of  $T_o$ .

To compute  $P$  as a function of  $T$ , we start with the differential form of the first law of thermodynamics (cf. Ref. A-1)

$$dh = dq + \frac{dP}{\rho}$$

In an adiabatic flow  $dq$  is zero, and dividing both sides by  $dT$  we get

$$\frac{dh}{dT} = \frac{dP}{\rho dT} \equiv C_p(T)$$

$$\rho = P/RT$$

so we can write

$$\frac{dP}{P} RT = C_p(T) dT$$

Dividing both sides by  $T$  and integrating

$$R \int \frac{dP}{P} = \int \frac{C_p(T)}{T} dT$$

Using the same fourth order polynomial for  $C_p(T)$  we have

$$\frac{C_p(T)}{T} = AT^3 + BT^2 + CT + D + \frac{E}{T}$$

Integrating from  $T_1$  to  $T_o$  we get

$$R \ln \frac{P_o}{P_1} = \frac{A}{4} (T_o^4 - T_1^4) + \frac{B}{3} (T_o^3 - T_1^3) + \frac{C}{2} (T_o^2 - T_1^2) + D(T_o - T_1) + E \ln \frac{T_o}{T_1}$$

Again, for any assumed value of  $T_o$ , a  $P_o/P$  versus  $T$  table can be computed.

Because we are dealing with gases where  $C_p$  is only a function of temperature, and not of pressure, any arbitrary value of  $P_o$  (the stagnation pressure) may be assigned. Figure A-1 shows a plot of  $C_p$  versus  $T$  for the gas used in the present investigation (42 percent Argon + 58 percent Freon 13B1), and Table A-1 gives the thermodynamic variables calculated by the above procedure for  $T_o = 487^\circ K$ .

#### Reference

- A-1 Liepmann, H. W. and Roshko, A., Elements of Gasdynamics, John Wiley and Sons, Inc., New York, 1957.

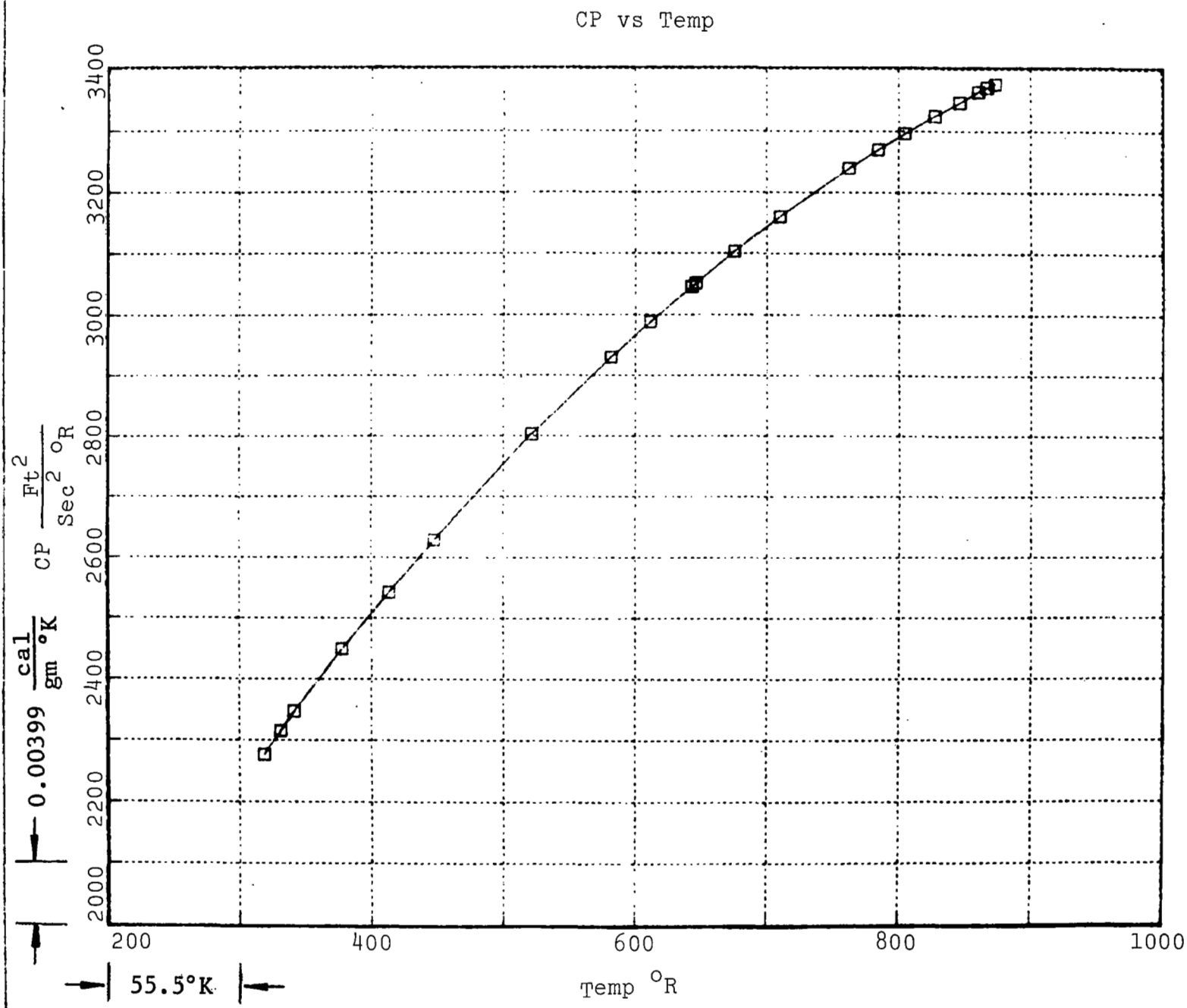


Fig. A-1 Variation of  $C_p$  with Temperature for Mixture of 42% Argon and 58% Freon 13B1

TABLE A-1 THERMODYNAMIC PROPERTIES OF  
42% ARGON - 58% FREON 13B1 SUBSTITUTE GAS MIXTURE

Molecular Weight = 103.15

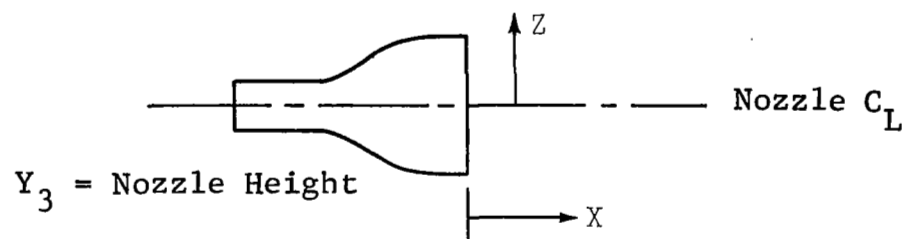
Mach Number	$\gamma$	T(°K)	$C_p \left( \frac{\text{cal}}{\text{gm}^\circ\text{K}} \right)$	P/P <sub>o</sub>
5.10682	1.32673	122.2	0.0781	5.29211E-04
4.74929	1.30558	138.9	0.0822	9.01289E-04
4.53703	1.29338	150.0	0.0848	1.25870E-03
4.24883	1.27738	166.7	0.0886	2.02347E-03
4.07301	1.26799	177.8	0.0911	2.73485E-03
3.75187	1.25169	200.0	0.0957	4.84265E-03
3.53212	1.24124	216.7	0.0990	7.25999E-03
3.26049	1.2292	238.9	0.1032	1.21256E-02
3.00744	1.21892	261.1	0.1072	1.97157E-02
2.76802	1.21006	283.3	0.1109	3.13131E-02
2.59493	1.20419	300.0	0.1135	4.36939E-02
2.36984	1.19725	322.2	0.1168	6.70062E-02
2.20341	1.19261	338.9	0.1192	9.12828E-02
1.98178	1.1871	361.1	0.1221	0.135923
1.8135	1.1834	377.8	0.1242	0.181417
1.69915	1.18113	388.9	0.1255	0.218947
1.58214	1.179	400.0	0.1268	0.263343
1.4614	1.177	411.1	0.1280	0.315699
1.33552	1.17513	422.2	0.1291	0.377259
1.20248	1.17338	433.3	0.1302	0.449431
1.13236	1.17254	438.9	0.1308	0.489986
1.05915	1.17174	444.4	0.1313	0.533804
0.982106	1.17096	450.0	0.1318	0.581116
0.811892	1.16948	461.1	0.1328	0.68721
0.604526	1.16811	472.2	0.1337	0.81039
0.471975	1.16746	477.8	0.1342	0.879117
0.287662	1.16684	483.3	0.1346	0.953027
0	1.16648	486.7	0.1348	1.00000

APPENDIX B

EXPERIMENTAL PRESSURE DATA NORMALIZED BY  
NOZZLE EXIT PRESSURE,  $\dot{p}_3$

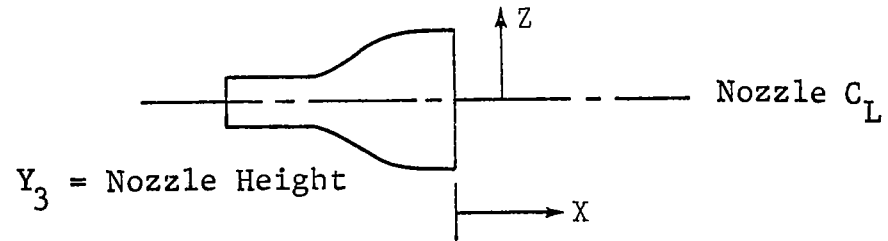


TABLE B-1 CONFIGURATION: COMBUSTION GAS, NO SIDE PLATES, NO STEP AT NOZZLE EXIT



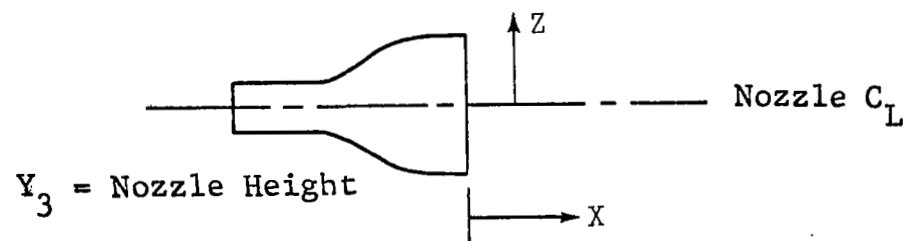
Afterbody			Afterbody			Cowl		
$X/Y_3$	$Z/Y_3$	$P/P_3$	$X/Y_3$	$Z/Y_3$	$P/P_3$	$X/Y_3$	$Z/Y_3$	$P/P_3$
0.485	0	0.276	4.406	-0.5	0.0780	0.833	0	1
1.426	0	0.273	4.406	0.5	0.0762	1.75	0	0.647
2.367	0	0.254	5.347	0.5	0.0669	2.417	0	0.508
3.936	0	0.112, 0.132	8.014	-0.5	0.0240	0.333	-0.5	0.952
4.877	0	0.0990	8.955	0.5	0.0165	1.417	0.5	0.670
6.131	0	0.0611	0.485	1.0	0.261	0.833	-0.833	0.857
7.543	0	0.0271	0.485	-1.0	0.271	0.833	0.833	0.895
8.484	0	0.0154	1.426	1.0	0.243	2.417	-0.833	0.430
9.425	0	0.0110	2.367	-1.0	0.0802	2.417	0.833	0.404
10.837	0	0.0095	0.955	-1.5	0.0957	0.333	1.167	1.0
12.248	0	0.0078	3.465	-1.5	0.0461	1.417	1.167	0.380
13.660	0	0.0047	0.485	-2.5	0.0008	0.833	-1.5	0.319
15.072	0	0.0038	1.426	-2.5	0.0044	2.417	-1.5	0.199
16.800	0	0.0036	2.367	-2.5	0.0053			
18.522	0	0.0034	3.465	-2.5	0.0168			
0.955	0.5	0.262	4.877	-2.5	0.0172			
0.955	-0.5	0.269	6.131	-2.5	0.0240			
1.897	-0.5	0.225	8.484	-2.5	0.0172			
3.465	-0.5	0.109						

TABLE B-2 CONFIGURATION: COMBUSTION GAS, NO SIDE  
PLATES, REARWARD STEP AT NOZZLE EXIT



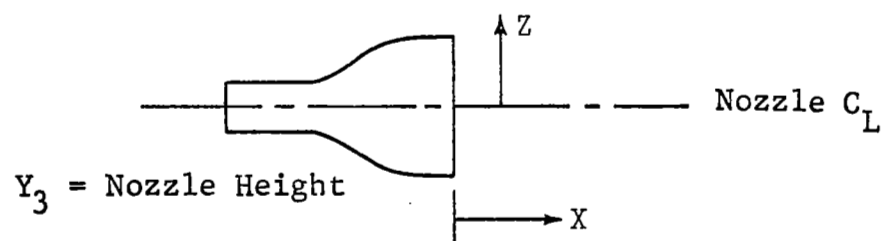
Afterbody			Afterbody			Cowl		
X/Y <sub>3</sub>	Z/Y <sub>3</sub>	P/P <sub>3</sub>	X/Y <sub>3</sub>	Z/Y <sub>3</sub>	P/P <sub>3</sub>	X/Y <sub>3</sub>	Z/Y <sub>3</sub>	P/P <sub>3</sub>
0.485	0	0.244	4.406	-0.5	0.0890	0.833	0	0.743
1.426	0	0.241	4.406	0.5	0.0817	1.75	0	0.530
2.367	0	0.229	5.347	0.5	0.0623	2.417	0	0.428
3.936	0	0.100	8.014	-0.5	0.0242	0.333	-0.5	0.517
4.877	0	0.0722	8.955	0.5	0.0185	1.417	0.5	0.604
6.131	0	0.0373	0.485	1.0	0.206	0.833	0.833	0.731
7.543	0	0.0389	2.367	-1.0	0.164	2.417	0.833	0.302
8.484	0	0.0178	3.465	1.0	0.100	2.417	-0.833	0.295
9.425	0	0.0082	0.955	-1.5	0.0729	0.333	-1.167	0.519
10.837	0	0.0070	3.465	-1.5	0.0524	1.417	1.167	0.274
12.248	0	0.0052	0.485	-2.5	0	0.833	-1.5	0.293
13.660	0	0.0048	1.426	-2.5	0.0037	2.417	-1.5	0.169
15.072	0	0.0052	2.367	-2.5	0.0115			
16.800	0	0.0042	3.465	-2.5	0.0120			
18.522	0	0.0028	4.877	-2.5	0.0183			
0.955	0.5	0.179	6.131	-2.5	0.0217			
0.955	-0.5	0.183	8.484	-2.5	0.0067			
1.897	-0.5	0.235						
3.465	-0.5	0.129						

TABLE B-3 CONFIGURATION: COMBUSTION GAS, SHORT SIDE PLATES, NO STEP AT NOZZLE EXIT

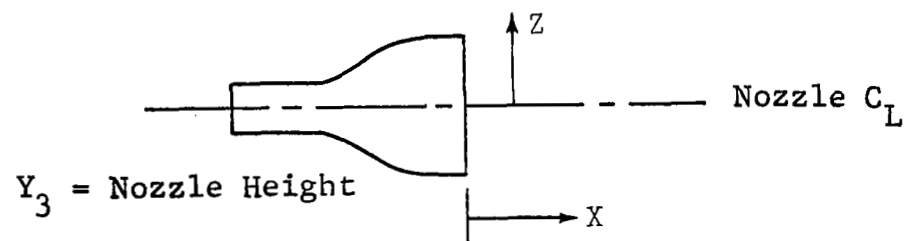


Afterbody			Gowl		
$X/Y_3$	$Z/Y_3$	$P/P_3$	$X/Y_3$	$Z/Y_3$	$P/P_3$
2.367	0	0.275	0.833	0	1.0
3.936	0	0.227	1.75	0	0.744
4.877	0	0.201	2.417	0	0.533
6.131	0	0.134	1.417	0.5	0.714
7.543	0	0.0610			
8.484	0	0.0428			
9.425	0	0.0354			
10.837	0	0.0231			
13.660	0	0.0142			
15.072	0	0.0131			
3.465	-0.5	0.193			
5.347	0.5	0.171			
2.367	-1.0	0.279			
3.465	1.0	0.152			

TABLE B-4 CONFIGURATION: COMBUSTION GAS, LONG SIDE PLATES, NO STEP AT NOZZLE EXIT

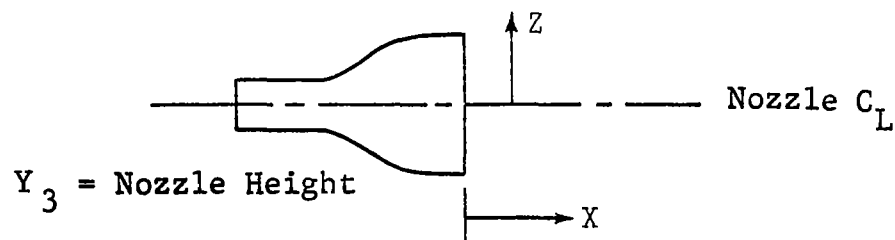


Afterbody		
$X/Y_3$	$Z/Y_3$	$P/P_3$
1.426	0	0.284
2.367	0	0.295
3.936	0	0.233, 0.234
4.877	0	0.230
6.131	0	0.161
9.425	0	0.105
10.837	0	0.0790
13.660	0	0.0352
3.465	-0.5	0.225
4.406	0.5	0.255
5.347	0.5	0.173
3.465	1.0	0.207

TABLE B-5 CONFIGURATION: SUBSTITUTE GAS, SHORT SIDE PLATES,  $M = 2.4$  NOZZLE

Afterbody			Cow1		
$X/Y_3$	$Z/Y_3$	$P/P_3$	$X/Y_3$	$Z/Y_3$	$P/P_3$
0.485	0	0.275	0.833	0	0.998
1.426	0	0.285	1.75	0	0.683
2.367	0	0.280, 0.250	2.417	0	0.483, 0.503
3.936	0	0.235	0.333	-0.5	0.945
4.877	0	0.268, 0.265, 0.270	1.417	-0.5	0.685
6.131	0	0.183	1.417	0.5	0.713
7.543	0	0.0825	0.833	0.833	0.868
8.484	0	0.0500	2.417	0.833	0.350
9.425	0	0.0475	2.417	-0.833	0.420
3.465	-0.5	0.316	0.333	1.167	1.18
4.406	0.5	0.320			
2.367	-1.0	0.320			
3.465	1.0	0.308, 0.310			

TABLE B-6 CONFIGURATION: SUBSTITUTE GAS, SHORT SIDE PLATES,  $M = 2.55$  NOZZLE



Afterbody			Cowl		
$X/Y_3$	$Z/Y_3$	$P/P_3$	$X/Y_3$	$Z/Y_3$	$P/P_3$
0.485	0	0.215	0.833	0	0.723
1.426	0	0.178, 0.168	1.75	0	0.605
2.367	0	0.235, 0.240	2.417	0	0.513
3.936	0	0.215	0.333	-0.5	0.703
4.877	0	0.195, 0.195	0.833	-0.833	1.36
6.131	0	0.110	2.417	0.833	0.413
7.543	0	0.0675	2.417	-0.833	0.373
8.484	0	0.06, 0.075	0.333	1.167	0.765
9.425	0	0.0475			
0.955	-0.5	0.213			
0.955	0.5	0.195			
1.897	-0.5	0.183			
3.465	-0.5	0.195			
4.406	0.5	0.173			
4.406	-0.5	0.198			
3.465	1.0	0.198			